



Quantitative surface characterisation and stress concentration of additively manufactured NiTi lattice struts

Mengna Zheng¹ · Kazem Ghabraie¹ · Yu-shuang Yang² · Joe Elambasseril³ · Wei Xu¹ · Yanan Wang¹

Received: 16 August 2023 / Accepted: 10 January 2024 / Published online: 19 January 2024
© The Author(s) 2024

Abstract

With the advancement of metal additive manufacturing (AM), lattice structures become a promising solution to situations that require lightweight design and yet maintain adequate mechanical strength. Limited by the quality of feedstock materials, the layer-wise process characteristic and the dynamic nature of thermal environment, lattice structures made by AM often suffer from process-induced imperfections such as poor surface finish and notable geometric deviation. In this study, systematic quantitative characterisation methods are developed to address surface quality and geometric discrepancy of NiTi lattice struts made by laser powder bed fusion (LPBF), with a special focus on fatigue-related features such as stress concentration factors. The results show that for the examined strut diameters and inclination angles, the strut diameter plays a significant role in geometry inaccuracy and the inclination angle has a greater effect on surface texture and stress concentration factor distribution on the surface. Lattice struts with diameters greater than 0.7 mm and inclination angles over 40° with respect to the platform exhibit superior manufacturing quality among all configurations of the struts. The proposed approach not only opens a new avenue to evaluate μ -CT data in a more quantitative way but also offers opportunities to develop guidelines for lattice structure design.

Keywords NiTi alloy · Laser powder bed fusion · Lattice structure · Surface roughness · Stress concentration factor

1 Introduction

In recent years, lattice structures have attracted increasing interest in designing and manufacturing for various applications in the aerospace and biomedical sectors [1]. They are constructed by arrays or other spatial arrangements of unit cells in both two and three dimensions [2], maintaining outstanding mechanical performance while being lightweight. Unlike subtractive manufacturing, additive manufacturing (AM) particularly laser powder bed fusion (LPBF) is a layer-wise freeform fabrication technique, which enables

the build of lattice structures with intricate geometries that are unachievable by traditional manufacturing methods. Featured with a number of attributes such as small achievable minimum feature, layer thickness, higher resolution and better surface finish, LPBF is commonly used for metal lattice structure fabrication.

With the nature of layer-by-layer processing, LPBF presents some inherent defects such as minor to moderate dimensional inaccuracy/geometrical variation, internal porosity and rough surface finish (surface defects) [3]. Internal porosity denotes the absence of material inside the intended solid geometry, which often occurs due to gas entrapment or the lack of fusion during the printing process [4, 5]. Dimensional inaccuracies refer to the geometric discrepancy of shape [6–8], size [9–11] or volume [12, 13] from the designed model, which is highly associated with the staircase effect and geometric overhang (inclination angle). Surface defects imply the deviation of the fabricated surface from the ideal or intended surface texture or quality [9, 10, 14–16], usually relating to the powder size, processing parameters, overhang and build orientation [10, 17–20]. Such defects can considerably affect the fatigue performance

✉ Wei Xu
wei.xu@deakin.edu.au

✉ Yanan Wang
yanan.wang@deakin.edu.au

¹ School of Engineering, Deakin University, Geelong, Victoria 3216, Australia

² CSIRO Manufacturing, Clayton, Victoria 3169, Australia

³ Centre for Additive Manufacturing, School of Engineering, RMIT University, Melbourne, Victoria 3000, Australia

of lattice structures [15, 16], which is essential for applications undergoing cyclic loadings such as bone implants [21, 22]. For instance, the geometrical discrepancy results in non-uniform stress distribution which is prone to initiate cracks; internal pores and surface defects are immediate/direct stress concentrators [23, 24] (cracks initiate at surface irregularities). Therefore, minimising such LPBF manufacturing imperfections is vital for designed lattice structures to maintain an adequate fatigue strength.

The most effective approach to reduce the internal porosity of LPBF-fabricated components is process optimisation, capable of achieving less than 1% internal porosity [25]. Post-LPBF treatment such as hot isostatic pressing (HIP) in conjunction with stress relief (SR) [26] can further densify the structure to near full density which provides sufficient enhancement on fatigue strength (28%) and endurance limit (83%) of lattice structures [27]. In contrast, the improvement of geometric and surface defects is limited using HIP and process optimisation due to the staircase effect inherent to the layer-wise processing. Surface post-treatments such as machining, sandblasting and abrasive polishing are often conducted to remove unwanted material and obtain a smooth surface for solid and regular shape pieces [28, 29]. However, for complex lattice structures, those treatments suffer from their inability to access or effectively/successfully reach the interior features of intricate geometries [30, 31].

Adapting a liquid agent such as chemical etching (CE) and electro-polishing (EP) has been applied successfully to reduce the surface roughness of the individual as-built lattice struts [9, 32, 33], characterised in surface roughness parameters (SRPs), e.g., Ra (profile arithmetic mean height), Rv (profile mean pit depth) [34] and Sq (areal root-mean height) [35]. There remain challenges in processing simple lattice structures such as BCC and cubic. For instance, it is difficult to maintain a uniform surface polishing from the exterior to the interior [31] and excessive material removal cannot be completely avoided, which results in broken struts ([36]—Fig. 4). A combination of HIP and CE can increase the local maximum stress of the LPBF diamond lattice at 10^6 run-out cycles [26], indicating that improving the ductility of material via heat treatment enhances fatigue strength. However, the improvement of fatigue endurance limit using CE shows inconsistent results in another study [14]. This is because CE or EP may not be able to effectively remove the surface micro-notch features which serve as stress concentrators [14]. The balance between excessive material removal [30] and sufficient surface smoothness from CE should be investigated and controlled carefully. Moreover, the reduction of surface roughness parameter values such as Ra and Sa does not result in an improvement of fatigue strength when critical defects persist [37]. This suggests that surface roughness parameters are not adequate to entirely characterise the surface quality when fatigue is concerned [18].

To overcome the limitations of post-treatments because of their inability to uniformly polish the interior surface and smoothen micro-notches without leading to broken struts, design constraint is another essential approach to alleviate AM geometrical and surface imperfections [3]. Prior to lattice structure fabrication, understanding the manufacturable inclination angles and diameters of lattice struts can avoid unnecessary failure builds such as broken struts or large geometric deviation [38–42]. By properly selecting strut diameter, pore size and relative density of the lattice unit cell, the overall geometric deviation can be reduced to below 10% [43]. A few attempts have explored the geometry and surface defects of lattice struts about particular strut orientation angles [9, 10, 44, 45] with special surface characterisation on SRPs (Ra, Rv and Sa) [34]. However, they lack statistical and quantitative characterisations of surface features in terms of the fatigue property. Moreover, little attention has been paid to the effect of strut diameter on surface quality.

The purpose of this study is to comprehensively evaluate AM manufacturing defects of lattice struts in various strut diameters and inclination angles, with a special focus on surface defects critical for fatigue. Here we propose a new approach to quantify the notch-like surface defects through stress concentration factors (SCFs). Using this in-depth analysis, the manufacturability of lattice struts is evaluated with respect to fatigue. Such systematic investigation reveals the relationship between design elements (inclination angle and diameter) and AM manufacturing quality in terms of internal porosity, geometry and surface defects.

In this study, the material of interest is NiTi (nitinol), a shape memory alloy extensively used in biomedical industries due to its unique shape memory effect and superelastic behaviour. It is important to investigate the design flexibility of NiTi lattice structures because it has an elastic modulus closer to human bone than commonly used implant materials such as titanium alloys [46–48]. Here an efficient and user-friendly surface quantification method has been developed to aid in the future design of reliable NiTi lattice structures with superior fatigue performance.

2 Material and method

2.1 LPBF specimen design and fabrication

The most broadly studied lattice structures are based on cylindrical struts and the individual struts in such lattices vary in both diameter and spatial orientation. Therefore, cantilever struts of different inclination angles and diameters were evaluated to gain a comprehensive understanding of the manufacturability of LPBF-fabricated NiTi alloys. Strut inclination angles of 10–60° and diameters ranging from 0.2 to 1 mm were considered, with increments of 10° and

0.1 mm, respectively (Fig. 1). The selection of strut diameter and the inclination angle is comparable with the minimum achievable feature of LPBF and previous work in the literature [38–42]. The inclined angle over 60° is not considered as the print quality shows marginal variations and they are expected to be successfully manufactured [44]. The 10 mm strut length is intended to cover all the common unit cell sizes found in the literature.

Spherical Ni50.2Ti49.8 (at%) alloy powder with particle size in the range of 15–53 μm was used for printing the designed NiTi struts under an inert argon atmosphere using a LPBF facility (SLM 125HL®, SLM Solutions). Six specimens were 45° aligned to the edge of the substrate to reduce the influence of the potential unsuccessful print between specimens. A total of 54 struts were manufactured on a preheated NiTi substrate (200 °C) using a Chessboard Island scanning strategy with a 67° angle increment between consecutive layers and the scan directions within each island are kept to x- and y-direction. The processing parameters used in this work (listed in Table 1) are defined in a previous processing parameter optimisation study which aims to obtain the maximal densification. The highest relative density achieved in the optimisation study is 99.89%.

The manufactured lattice struts were removed from the base plate using electrical discharge machining (EDM). The loose powder attached to the struts was first brushed off and then vacuumed off. All specimens were ultrasonically cleaned prior to the CT scan to minimise measurement error.

2.2 X-ray computed tomography

X-ray computed tomography (micro-CT/ $\mu\text{-CT}$) is a sample non-destructive technique for imaging 3D geometries of both interior and exterior features of solid objects in a

digital format. It has been successfully applied to dimensional quality control of AM parts in the industry and AM surface tomography evaluation [49]. Compared to other surface characterisation methods such as variation and confocal microscopy, $\mu\text{-CT}$ is able to acquire surface information and re-entrant features with greater accuracy [50, 51].

In this study, each specimen was scanned using a metrological $\mu\text{-CT}$ system (Phoenix datos 2). The scan was performed with a tube voltage of 180 kV and a current of 65 μA and an effective voxel size of 12 μm . The mean height (Ra) of LPBF-manufactured surface ranges from 16 to 35 μm [52], so the $\mu\text{-CT}$ scan with 12 μm voxel size is capable to capture most of the key surface features of the lattice struts. For each scan, a total of 1200 16-bit projection images were acquired during a 360° rotation, and the 3D tomographic slices were reconstructed using VGstudio MAX 3.

2.3 $\mu\text{-CT}$ data post-processing

The reconstructed 3D slices for each sample were exported from VGstudio in 16-bit TIFF image format. Using the 3D CT slices as constraint data, 3D porosity distribution in a sample was obtained with a data-constrained modelling (DCM) method. Further surface analysis was carried out with MATLAB. The following sections describe the analysis procedures of the collected image data from the CT scan for quantitative investigation of the manufacturing quality.

DCM is a software platform for 3D material modelling, characterisation and visualisation [53–55]. In this study, the porosity analysis is performed using DCM due to its capability of detecting partially-porous voxels of micro- or nano-porosity that is smaller than the $\mu\text{-CT}$ resolution. Each strut was separated after importing into DCM for porosity analysis. The sample boundary was built based on 0.7 times the threshold value

Fig. 1 CAD illustration of samples for cantilever lattice struts.

a Iso view of the 60° sample;
b front view showing all the 6 printed samples with 6 different strut angles;
c top view of the 60° sample showing the different strut diameters

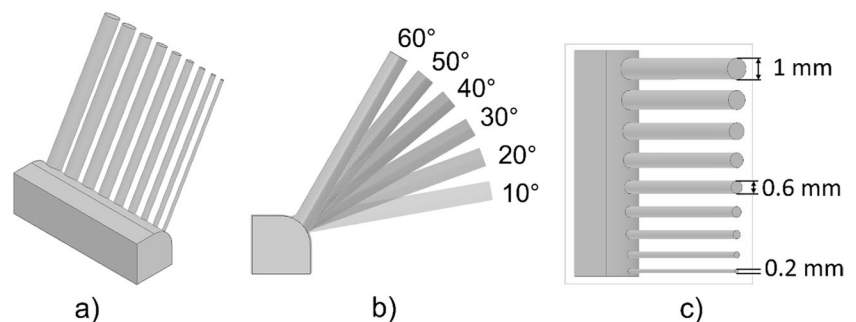


Table 1 LPBF processing parameters used in this study

| Laser power (W) | Layer thickness (μm) | Scanning speed (mm/s) | Hatch spacing (μm) | Focal offset distance (mm) | Inter-layer time (s) | Point distance (μm) | Exposure time (μs) | Energy density (J/mm^3) |
|-----------------|-----------------------------------|-----------------------|---------------------------------|----------------------------|----------------------|----------------------------------|---------------------------------|---|
| 200 | 30 | 875 | 120 | 0 | 5 | 70 | 80 | 63.5 |

of the CT slices. The beam hardening effect was alleviated using the moving volume averaging method [56] in the DCM software for each strut. The porosity was calculated inside the sample boundary. Clustering of internal voids was calculated with the assumption that two neighbouring voxels are connected when both of their void volume fraction is over 7% of the voxel size.

To characterise the geometry and surface features of the specimen, the point data of the boundary pixels for each strut was extracted from DCM by a self-developed plug-in. The surface information (surface pixels point cloud) is extracted based on the above sample boundary. Afterwards, the point cloud data of each strut was analysed with an in-house developed MATLAB routine.

2.3.1 Geometric variation analysis

To characterise the geometric inaccuracy of the manufactured struts from designed parameters, a circular cylindrical (Cir) fitting was applied to the point cloud data of all struts. The shape of the effective fitted surface was considered as a representation of the manufactured sample. The dimensionless (normalised) size discrepancy is evaluated by the variation between the fitted diameter and designed diameter as Eq. 1.

$$d_{size} = \frac{|r_d - r_f|}{r_d} \times 100\% \quad (1)$$

where r_d and r_f are the designed and circular fitted radius of each strut.

From the literature, the cross-section of the AM fabricated cylindrical samples can exhibit an elliptical shape [7, 10, 57]. The shape deviation can lead to off-axial loading and anisotropic behaviour which can significantly impact the static and dynamic performance of LPBF-manufactured components. From the optical assessment (Section 3.1) and visualisation of the reconstructed μ -CT projections, this phenomenon is obvious among the printed samples, especially on struts with smaller diameters. To evaluate such shape discrepancy, the boundary point cloud was further fitted to an equivalent elliptical cylinder (Ell) and the ellipse axes was utilised to calculate the shape discrepancy as Eq. 2.

$$d_{shape} = \left(\frac{a}{b} - 1 \right) \times 100\% \quad (2)$$

where a and b are the semi-major and semi-minor axes respectively of the elliptical fitted cylinder of each strut.

2.3.2 Surface characterisation

Based on the point cloud data extracted from μ -CT with DCM, the surface quality of each strut was characterised in the following three steps:

- 1) Surface tomography mapping
- 2) Surface roughness analysis
- 3) Stress concentration analysis

A detailed workflow of the developed methods is illustrated in Fig. 2.

In surface tomography mapping, pixel data of each strut was unfolded based on the effective equivalent surface of the Cir and Ell fitting. The central axis of the fitted cylinder was first computed. The angle projection of the point cloud data to the perpendicular plane of the axis was identified to determine the unfolded location of the μ -CT pixel data along the strut circumference. The unfolding process maps the point data into a flat tomography surface and preserves the distance between the effective fitted surface and the point data from the μ -CT results. Areal SRPs such as mean Sa, square-root Sq, maximum peak height Sp, maximum pit depth Sv and maximum peak to valley height Sz were obtained based on the surface tomography mapping as defined in ISO 25178-2 and ISO 21920-2 [35, 58]. A 2D robust Gaussian filter was applied before the computation to remove large-scale lateral components (L-filter [35]) from the surface and to eliminate any numerical errors during the CT scan. The cut-off value was set to 0.8 mm as recommended by ISO 25178-1:2016 [59]. As the unfolding process in surface tomography mapping has taken the form of the surface, the F-operation indicated in [35] was not performed further.

The stress concentration analysis is to overcome the limitation of the surface roughness analysis [18], in particular focusing on the characterisation of notch-like features. To avoid the excessive computational cost of finite element analysis (FEA) of each sample [60], an analytical approach was developed to calculate the SCF of each surface based on its surface tomography. This method is an extension of the most accepted single-notch SCF model as illustrated in Fig. 3 and formulated in Eq. 3 [61].

$$K_t = 1 + 2\sqrt{\frac{t}{\rho}} \quad (3)$$

where K_t is the single-notch elastic stress concentration factor and t and ρ are the notch depth and radius at the notch tip.

Surface segmentation was applied to the tomography mapping to define the significant surface features. The segmentation process consists of the identification of the valleys and peaks of the tomography surface followed by the determination of the hill and dale regions on the surface [35]. The watershed transformation was employed to compute the segmentation, which is a robust image segmentation method based on mathematical morphology [62]. Originating from geography, the watersheds are the dividing lines of surface domains formed when water naturally

Fig. 2 Workflow and expected outcomes of the geometric variation and surface quality analysis methods developed in this study

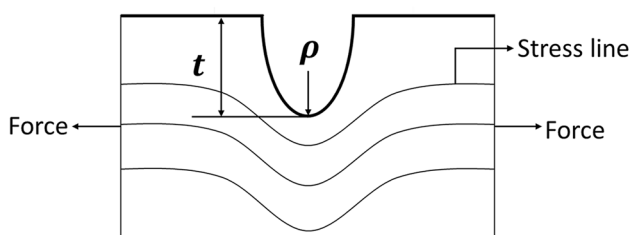
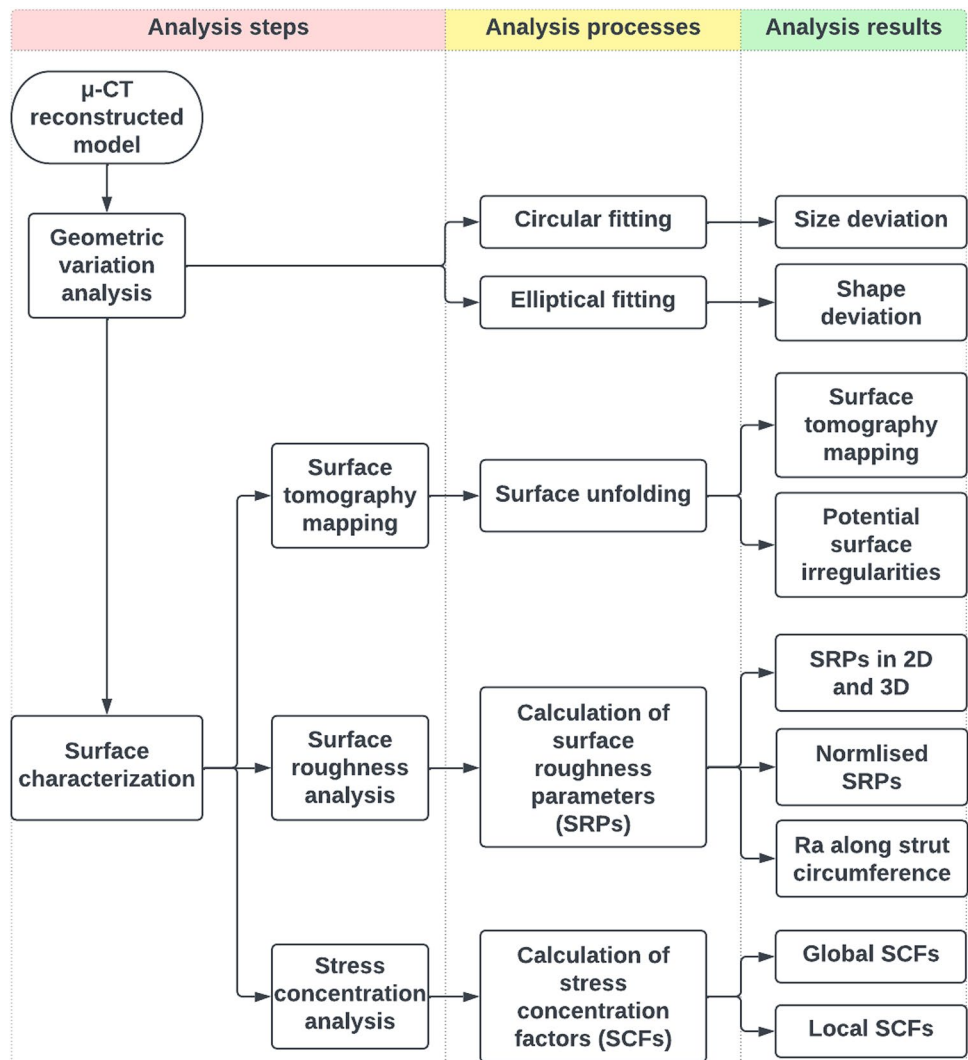


Fig. 3 Single-notch stress concentration model (adapted from [61])

flows down the steepest path of a landscape and falls into areas of attraction [63]. A previous study has pointed out that the SCFs calculated based on key contour features instead of micro-notch features showed a better correlation with the fatigue strength of the machined workpiece [64]. On the other hand, unconstrained watershed transformation usually results in ‘over-segmentation’ with numerous small segments. Therefore, introducing reasonable criteria

of size for segmentation to pruning our insignificant features are necessary to obtain a suitable surface segmentation, such as the Wolf pruning which eliminates a certain threshold value of specified height/depth or percentage of S_z [35]. In this study, the segmentation was performed with Wolf pruning 5% total height as the default value recommended by [59], but the threshold value can be altered for specific situations.

In a previous study [64], the key contour features were defined through the profile feature parameters specified in the geometrical specification standard for the profile [34]. To extend this concept, areal featured parameters such as S_{vc} (arithmetic mean pit curvature) and S_{10z} (ten-point height) were computed as defined in [35]. The global SCF of the surface can be calculated according to the areal featured parameters as formulated in Eq. 4. This global SCF is presumably a general indication of the fatigue property of the strut in terms of crack initiation.

$$K_{r,global} = 1 + 2 \sqrt{\frac{S_{10z}}{\frac{1}{S_{ve}}}} \quad (4)$$

The fatigue crack usually initiates where the stress concentrates, which is most likely where the critical notch is located. Therefore, the maximum local SCFs on the surface and their location on the surface were evaluated to obtain deeper insights into the stress concentration distribution over the surface. The locations of the local SCFs were defined as the valleys of the surface which were considered as stress concentrators. The values of the local SCFs were computed via Eq. 5, where D_v is the local valley depth as defined in [63] and ρ_v is the tip radius at the local valley. The values of the calculated surface roughness parameters and local stress concentration factors can be associated with the CT scan resolution or voxel size.

$$K_{r,local} = 1 + 2 \sqrt{\frac{D_v}{\rho_v}} \quad (5)$$

3 Results

3.1 Optical assessment

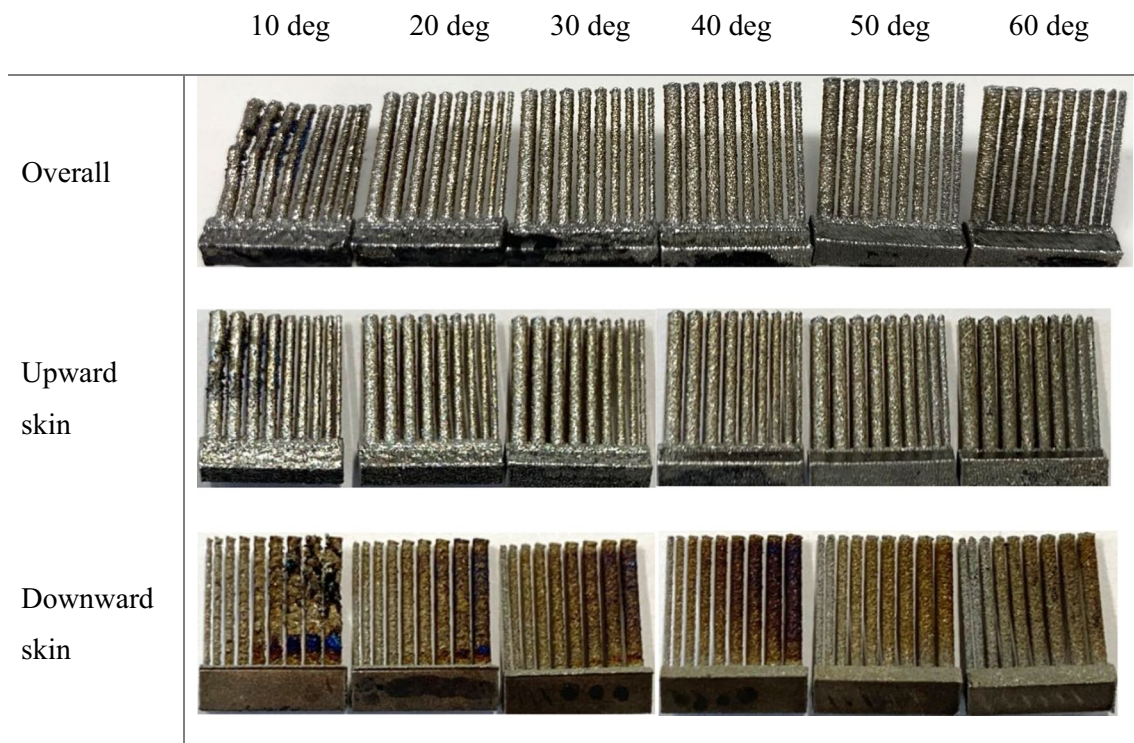
Unsuccessful builds at low inclination angles (10°) are expected based on previous studies on other materials

[38–40]. However, different printability is found with respect to the strut diameters at low inclination angles. Similar to H13 tool steel [40], NiTi struts present severe distortion when increasing strut diameter beyond 0.6 mm, such as bending in the middle. Conversely, materials like Ti-6Al-4 V, AlSi12Mg and Inconel 625 [38, 39] exhibit the opposite trend, suggesting that this behaviour is material dependent (Table 2).

The bending at the middle of the thicker struts for samples built along 10° can be observed. Such pronounced deformation can be mainly caused by lacking rigid connection between melted powders due to the low inclination angles. As such, residual stresses, structures built on loose powder beds or overhangs with less stability, and sintered powder from beneath loose powder beds can all contribute to the instability of the low inclination angle struts.

The upward skin is brighter in contrast and smoother compared to the downward skin. The better smoothness is possibly a result of melt pool geometry and the lack of successive powder deposition. This phenomenon was also reported in previous literature, where the downward skin has more loose particles attached to it compared to the upper skin [10]. The downward skin presents obvious colour changes compared to the original colour of NiTi, especially on thicker struts. This is likely due to possible oxidation taking place in areas undergoing more pronounced heat accumulation and overheating.

Table 2 LPBF manufactured NiTi samples at different diameters and orientation angles



The tip of the struts exhibits unexpected material accumulation, which may be because of the slicing effect resulting from the selected scanning strategy and might be minimised via optimising the scanning strategy, such as altering the scanning contour and laser path compensation [65]. To ensure the accuracy and consistency of the following analysis, such features were removed for all struts in the subsequent geometry and surface analysis. Overall, the result of the optical assessment is summarised in Table 3. Note that the visual optical judgement might be relatively subjective.

Due to the severe distortion of struts built at 10° for the diameter range of 0.7–1 mm, the struts built at 10° were left out from the rest of the characterisation to keep the results consistent. All struts examined had densities over 98% which confirms the suitability of the printing parameters and the print quality in terms of internal porosity.

Figure 4 illustrates an example of the reconstructed model in DCM and the extracted surface point data of the 0.9 mm strut. The downward-facing and upward-facing skins of the struts built at 60° are presented, where the downside exhibits rougher surfaces than the upper skin for all struts. The following analysis results are based on the

surface point data of each strut extracted from the reconstructed model (Fig. 4c).

3.2 Geometric deviation

Figure 5 shows the analysis procedures of the effective cylindrical fitting (Fig. 5a and b) in geometric deviation analysis and the unfolding process (Fig. 5c and d) in surface tomography mapping. The schematic illustration is based on circular fitting of 60° 0.9 mm strut and the elliptical fitting shares the same procedure. Figure 5b shows the top view of the top view of the point data and fitted surface with the surface areas (side, up and down) and unfolding parting line indicated. Both fittings determine the fitted surface by minimizing the point data distance between the fitted surface and the actual surface; therefore, the distance relationship between the point data and fitted surface is preserved.

The geometric deviation in terms of shape and size is presented in Tables 4 and 5, respectively, which were computed using Eqs. 1 and 2 according to the effective radius of the circular fitting and the major and minor axes of the elliptical fitting.

The shape deviation declines with an increase in strut diameter for all angles and shows more significant influence

Table 3 Manufacture quality of the as-built NiTi struts via optical assessment

| | | Strut diameter (mm) | | | | | | | | | |
|-----------------------------|----|---------------------|-----|-----|-----|-----|-----|-----|-----|-----|--|
| | | 0.2 | 0.3 | 0.4 | 0.5 | 0.6 | 0.7 | 0.8 | 0.9 | 1.0 | |
| Strut inclination angle (°) | 10 | YES | YES | YES | OK | OK | NO | NO | NO | NO | |
| | 20 | YES | YES | YES | YES | YES | YES | OK | OK | OK | |
| | 30 | YES | YES | YES | YES | YES | YES | YES | YES | YES | |
| | 40 | YES | YES | YES | YES | YES | YES | YES | YES | YES | |
| | 50 | YES | YES | YES | YES | YES | YES | YES | YES | YES | |
| | 60 | YES | YES | YES | YES | YES | YES | YES | YES | YES | |

‘NO’ represents major flaws including severe geometry deviation such as bending (shown in Table 2); ‘OK’ refers to moderate flaws such as large waviness of the downward surface; ‘YES’ corresponds to successful print

Fig. 4 Schematic of micro-CT reconstructed model and surface point data extraction procedure. **a** Downward-facing skin; **b** upward-facing skin; **c** surface point data

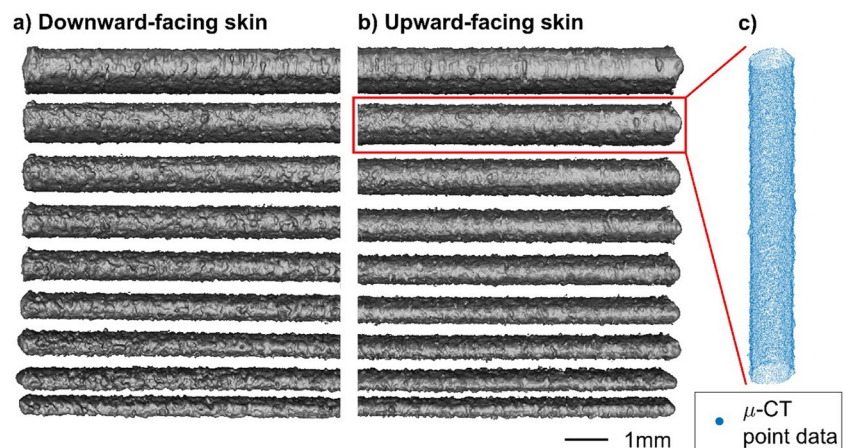


Fig. 5 Schematic of μ -CT surface point data geometric and surface tomography mapping procedure. **a** Iso and **b** top view of the μ -CT point data and fitted surface; **c** top view of the unfolded point data; **d** unfolded tomography mapping of the struts

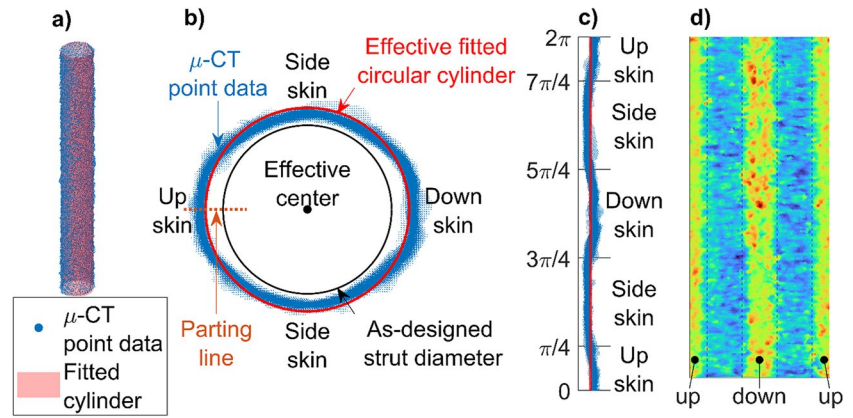


Table 4 Shape deviation (%) of the as-built NiTi lattice struts

| | | Strut diameter (mm) | | | | | | | | |
|-----------------------------|----|---------------------|-----|-----|-----|-----|-----|-----|-----|-----|
| | | 0.2 | 0.3 | 0.4 | 0.5 | 0.6 | 0.7 | 0.8 | 0.9 | 1.0 |
| Strut inclination angle (°) | 20 | 54% | 50% | 46% | 40% | 31% | 23% | 16% | 11% | 5% |
| | 30 | 42% | 44% | 39% | 34% | 27% | 23% | 18% | 15% | 10% |
| | 40 | 28% | 32% | 29% | 25% | 21% | 17% | 16% | 15% | 10% |
| | 50 | 25% | 39% | 32% | 29% | 26% | 23% | 21% | 17% | 9% |
| | 60 | 23% | 36% | 30% | 25% | 23% | 21% | 18% | 15% | 8% |

Table 5 Size deviation (%) of the as-built NiTi lattice struts

| | | Strut diameter (mm) | | | | | | | | |
|-----------------------------|----|---------------------|------|-----|-----|-----|-----|-----|-----|-----|
| | | 0.2 | 0.3 | 0.4 | 0.5 | 0.6 | 0.7 | 0.8 | 0.9 | 1.0 |
| Strut inclination angle (°) | 20 | 136% | 88% | 62% | 46% | 33% | 24% | 16% | 11% | 9% |
| | 30 | 138% | 86% | 61% | 44% | 32% | 25% | 19% | 15% | 13% |
| | 40 | 135% | 82% | 55% | 40% | 30% | 23% | 19% | 17% | 15% |
| | 50 | 156% | 104% | 67% | 49% | 38% | 31% | 25% | 21% | 16% |
| | 60 | 160% | 108% | 70% | 50% | 39% | 31% | 25% | 21% | 17% |

in lower-angle inclined struts. However, the strut diameters exhibit a more dominant effect on the shape deviation of smaller struts as the thicker struts generally have a stable shape deviation through all angles. This might be because the thinner struts have diameters closer to the powder size and the attached unmelted particles have more impact on its shape formation leading to more elliptical shape. Such a shape discrepancy has also been observed in the literature [7, 10, 66].

The size deviation shows a strong relationship with strut diameter, revealing a lower size discrepancy present in greater diameters. However, no clear relationship can be interpreted between the size deviation and the inclination angle. Figure 6 visualises the data in Tables 4 and 5. The size deviation shows a steep decreasing trend at small strut diameters and begins to level off when the strut diameter approaches 1 mm. This means that the shape of the fabricated struts is approaching the intended geometry in large struts.

3.3 Strut surface characterisation

3.3.1 Surface tomography mapping

Figures 7 and 8 present the surface tomography mapping of circular and elliptical fittings, respectively. The value of the colour bar represents the distance between the fitted effective surface and the μ -CT point data (mm). BD at the bottom left corner stands for build direction during the print. The short and long edges of each surface denote the circumference and length of the strut, respectively. All the surfaces were cut into the same length from the base for better presentation. The length of the short edge depends on the fitted parameters and therefore small variations between the lengths are expected. The middle of each surface mapping refers to the downward skin of each strut and the two long side edges represent the upward skin. The slight fluctuation in circumference (short edges) for a specific diameter is due to the variation of the effectively

Fig. 6 Geometrical deviation between designed and manufactured struts. **a** Shape deviation (calculated via Eq. 1); **b** size deviation (calculated via Eq. 2)

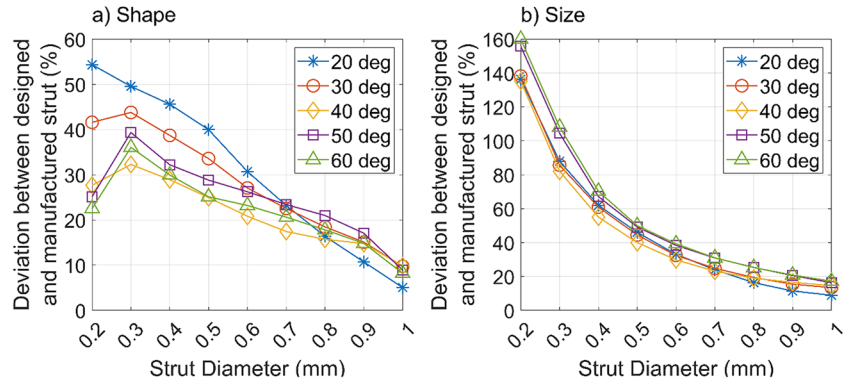


Fig. 7 Unfolded surface tomography mapping via circular fitting of the as-built NiTi struts

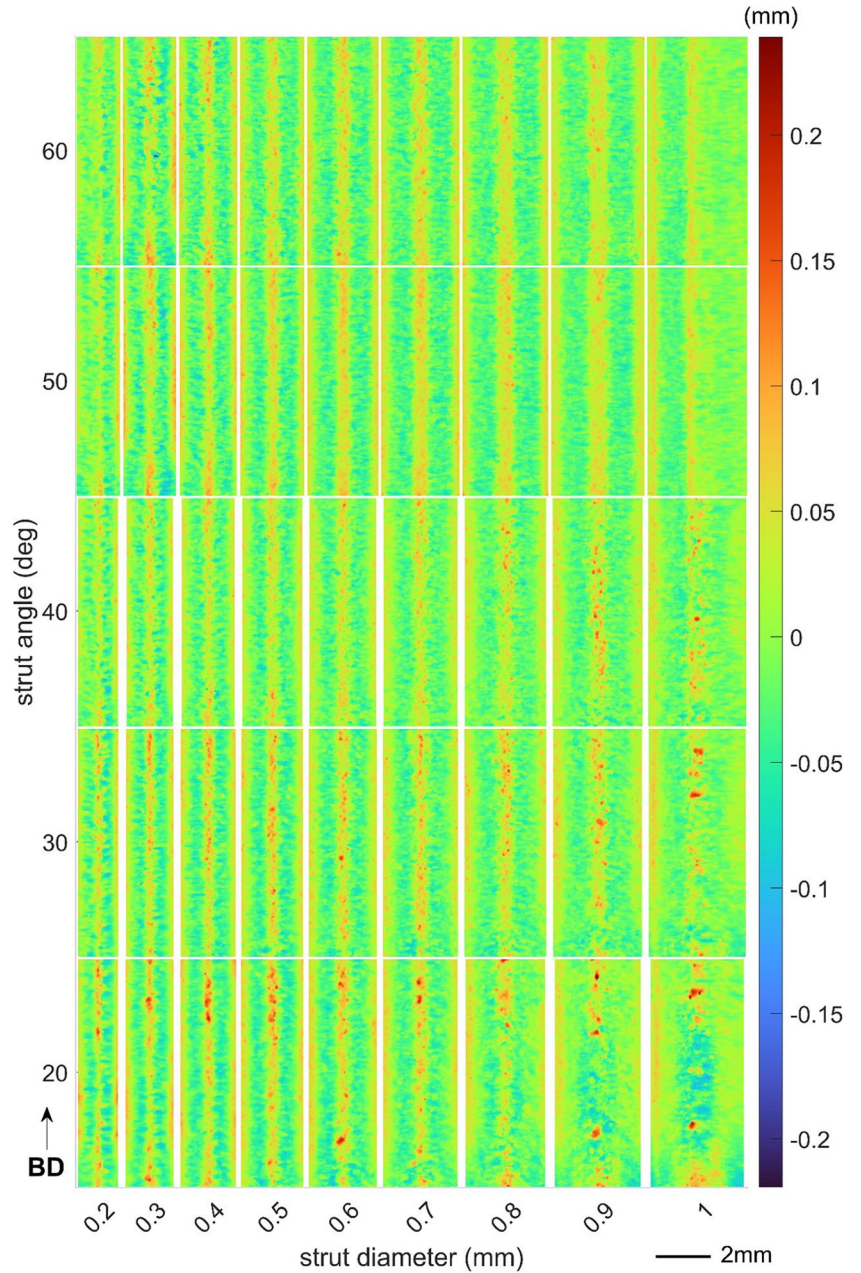
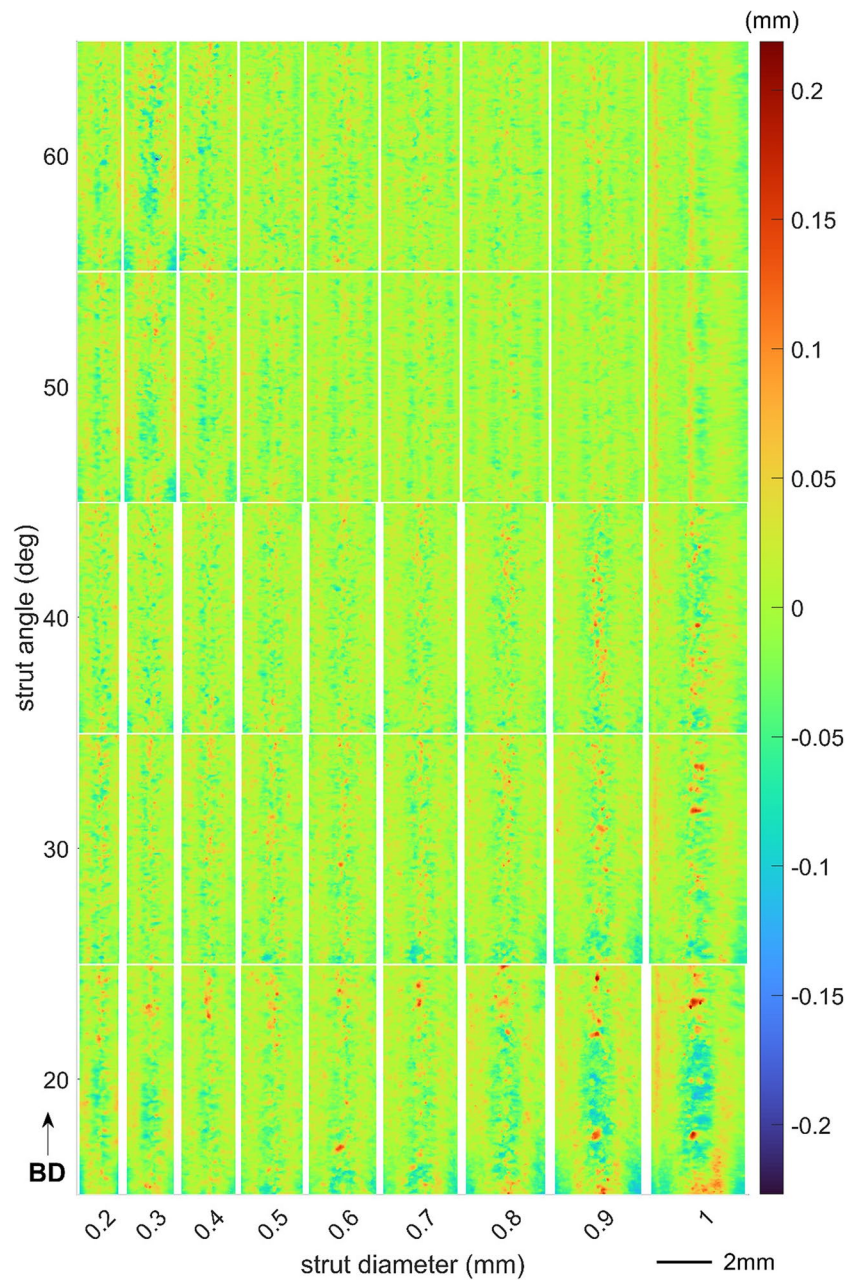


Fig. 8 Unfolded surface tomography mapping via elliptical fitting of the as-built NiTi struts



fitted diameter of struts, as indicated by the size deviations in Table 5.

Surface tomography mappings of circular fitting present clear rougher surfaces in the downward and upward skin areas, whereas elliptical fitted tomography mappings do not show the same phenomenon on the upward skins. This aligns with the results of the previous geometric analysis where the shape of the struts is more elliptical rather than circular as designed, especially for those made at small inclination angles and strut diameters. The tomography mappings of both fitting methods capture similar key rough features in 20° struts and thicker struts in 30°/40° on the downward skin regions. Compared to struts built with lower inclination

angles, 50° and 60° struts exhibit a more uniform surface texture around the circumference.

Abnormal concave areas can be discerned in 20° thicker struts (0.7–1.0 mm). Such strut waviness might be due to the development of greater residual stress originating from excessive heat accumulation and overheating in builds along lower inclination angles. Moreover, the surface mappings of the as-built NiTi struts do not show any noticeable variations along the length of the strut (build direction), indicating the length of the struts has little influence on the surface texture.

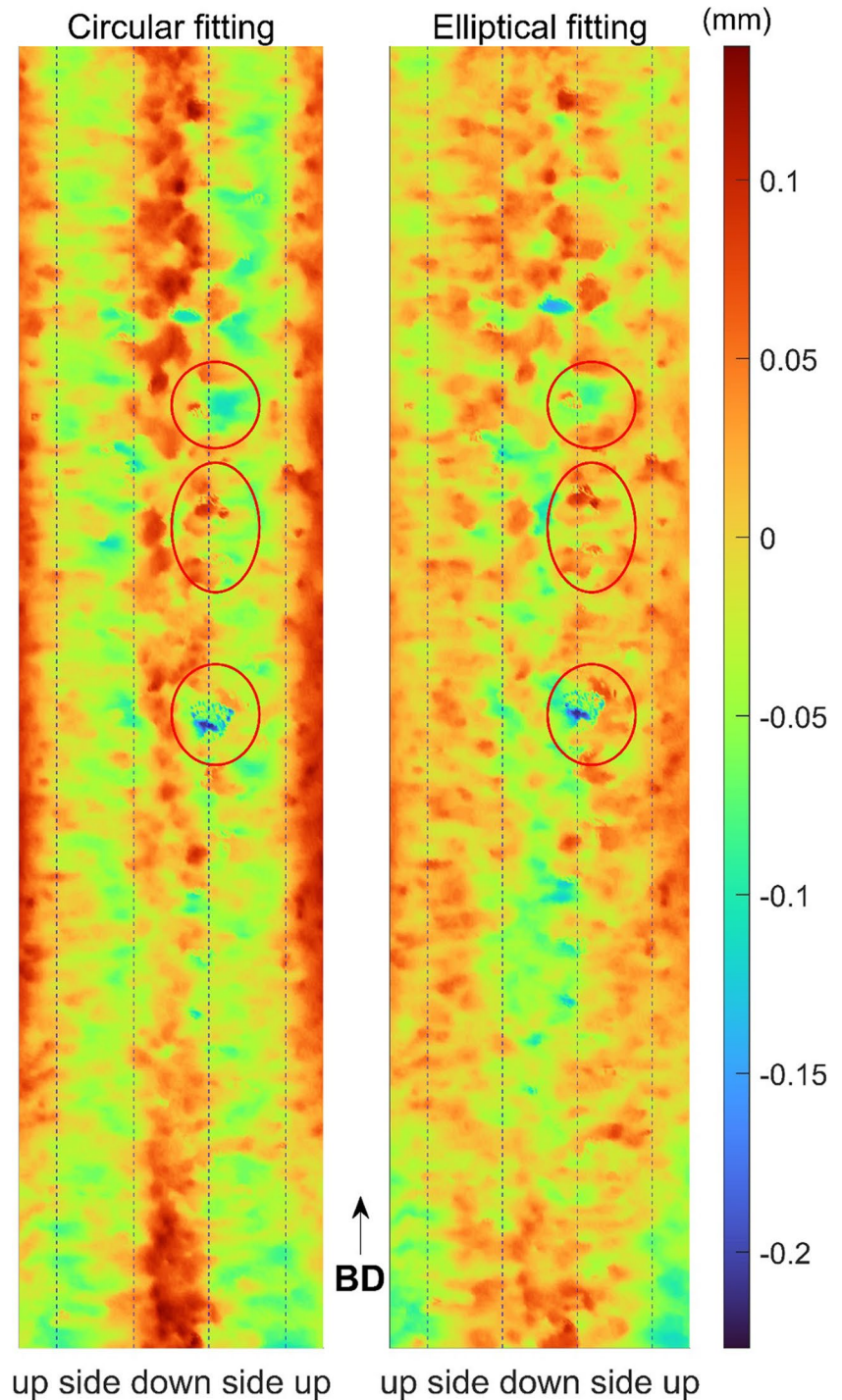
Figure 9 gives an example of the irregularity of the acquired μ -CT data. The dash lines separate the tomography mapping based on the skin areas, such as downward-facing

skin (down), lateral skin (side) and upward-facing skin (up). The red circle marks the pronounced irregular regions. Note that due to the difference in colour bar scale, the surface colour varies from tomography mapping for all struts (Figs. 7 and 8). BD at the bottom stands for build direction during the print.

The benefit of the surface tomography mapping is two-fold. One is to visually present the surface for each strut

to obtain an overview of the surface texture as discussed above and to prepare for subsequent surface quality analysis. The other is to intuitively assess the CT scan quality for any numerical error which may appear occasionally. For example, the 60° 0.3 mm strut exhibits noticeable irregularity in both peaks and valleys along the intersection line of the downward-facing skin and the lateral skin for both fitting methods (Fig. 9 annotated in red circles). Such irregularity

Fig. 9 Irregularity present in the acquired μ -CT data (possibly from the re-entrant features on the struts) in 60° 0.3 mm strut



may occur due to the uncertainty of the printing process such as the occurrence of the re-entrant features on the struts [50]. After the Gaussian filter operation, such irregularities are mostly removed. The tomography mapping of the same strut (60° 0.3 mm) after the Gaussian filtering is provided in supplementary material Figure S1 for comparison. The following results in Sections 3.3.2 and 3.3.3 are obtained based on the tomography mapping after the Gaussian filtering operation.

3.3.2 Surface roughness analysis

According to the geometric analysis above, all samples are closer to the elliptical shape. Therefore, the following surface roughness analysis is focused on the elliptical fitted effective surface which has a better representation of the surface texture.

Figures 10 and 11 depict the measurements of SRPs for all samples in 2D and 3D, respectively. The dashed contour in both figures illustrates the median value of all struts in each parameter category. Ra, Rq, Rz, Rp and Rz are mean, square-root, maximum peak to valley height, maximum peak height and maximum pit depth, respectively, for 2D profile and the same subscript follows for 3D areal parameters. The median value of each parameter category (dashed contour) is comparable with those in the literature [10, 14]. Although all parameters exhibit similar distribution among specimens, the maximum peak-to-valley depth (Rz) is six times higher

than the arithmetic mean values (Ra). This phenomenon is more evident in 3D areal parameters.

It was expected that lower inclination angles may result in rougher surfaces due to the residual stress mentioned earlier. However, an unexpected peak is observed around the 60° 0.3 mm strut, which may be a scan irregularity as previously discussed in Section 3.3.1. Overall, better surface quality was achieved in samples with higher inclination angles and thicker strut diameters. The acceptable range (roughness values lower than the reference line) roughly falls between struts built along 40° to 60° with 0.5–1.0 mm strut diameters.

The size of the powder used in this study is around $50\ \mu\text{m}$. When the powder size is closer to the intended geometry, any unmelted powder attached to the surface may have a significant influence on its surface quality. Moreover, the melt pool size and shape of the applied processing parameters can be around 80 to $100\ \mu\text{m}$ [67–69], which may also lead to the large shape and size deviation of the smaller struts. Therefore, it is reasonable to consider the effect of powder size and melt pool size on surface roughness. This effect was characterised by normalising the 3D SRPs to the designed and the equivalent fitted radius of the elliptical fitting, respectively. The equivalent fitted radius is defined as the mean value of the two semi-axes of the elliptical fitting.

Figure 12 presents the normalised Sa and Sq values. The equivalent fitted radius of the elliptical fitting in Fig. 12a is defined as the mean value of semi-major and -minor axes

Fig. 10 2D surface roughness parameters (SRPs) of all samples computed based on the effective elliptical fitted surface

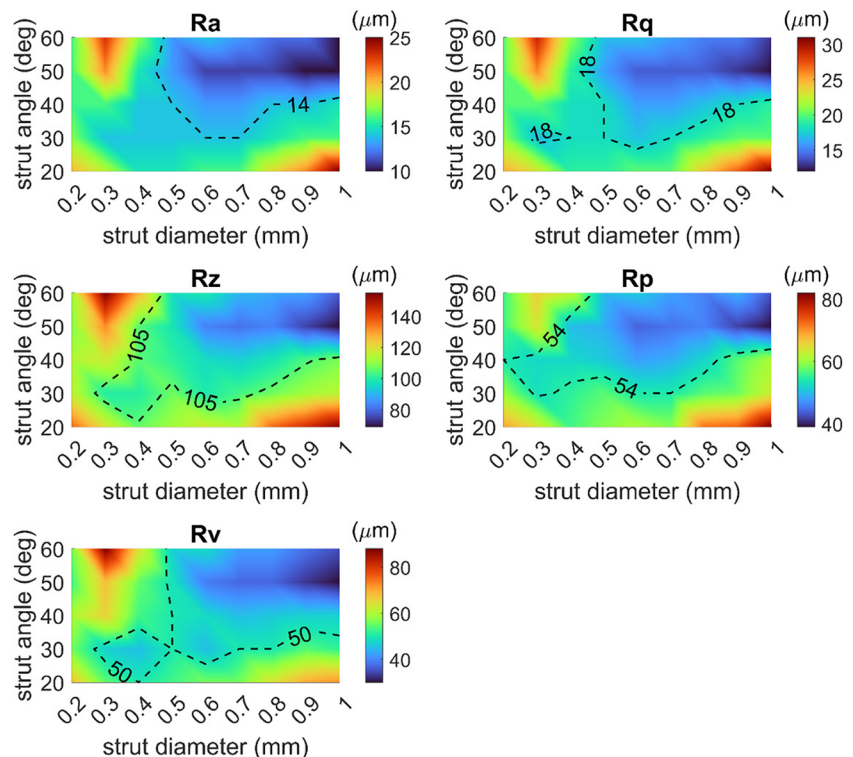
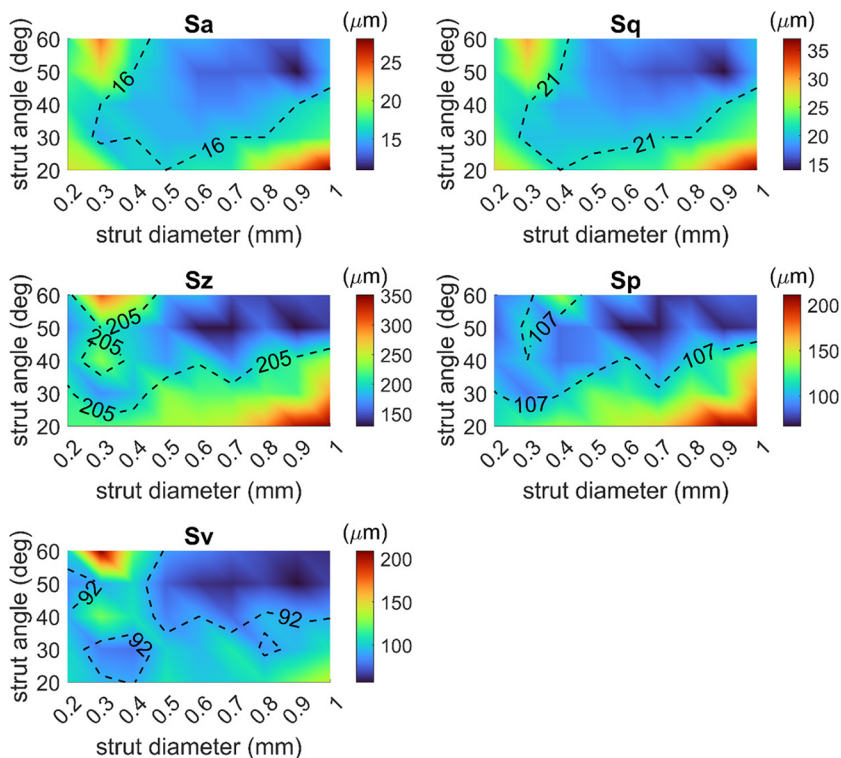


Fig. 11 3D surface roughness parameters (SRPs) of all samples computed based on the effective elliptical fitted surface

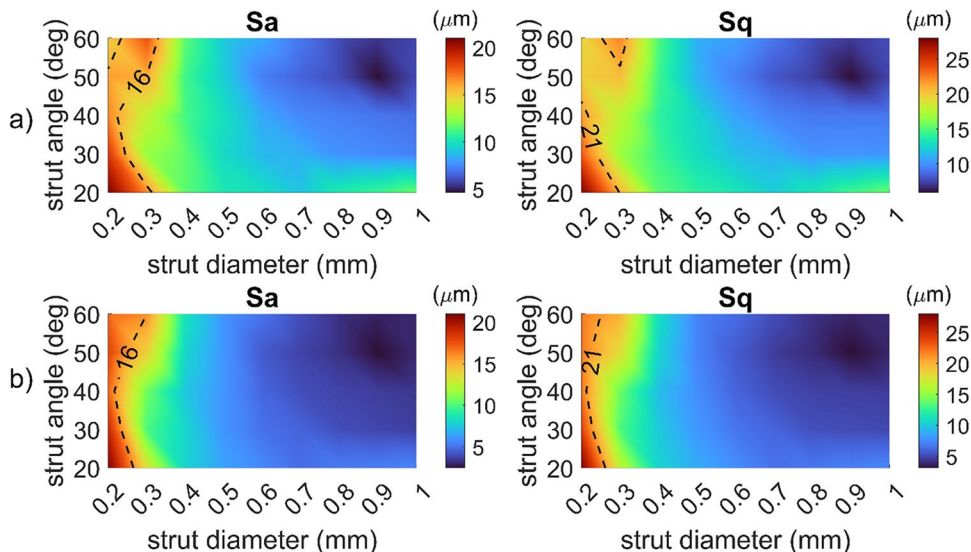


of the elliptical fitted effective surface. The radius was first normalised to the minimum value in the data set of all struts, and then normalised to the 3D surface roughness parameters, to make the normalised data to be comparable with non-normalised results in Fig. 11. The dashed lines exhibit the median value of the non-normalised results in Fig. 11. As expected, the normalised Sa and Sq remain high on small diameters (less than 0.4 mm) for both normalisation scenarios, which indicates the predominant influence of powder size on surface roughness. Therefore, a strut diameter of

less than 0.4 mm is not recommended for preventing such powder-size effects.

The above measurements on SRPs can only provide an overview of the surface quality rather than providing any quantitative information on local surface quality. To further characterise the surface quality in specific areas such as the overhang area (downward skin), the surface mapping was sliced around the circumference to form individual profiles along the strut length. Figures 13 and 14 illustrate the Ra values of all individual profiles around the circumference in

Fig. 12 Relative 3D surface roughness parameters (SRPs) of all samples computed based on the effective elliptical fitted surface. **a** Normalised to the fitted radius; **b** normalised to the designed radius



terms of strut diameter and inclination angle, respectively. The dash lines separate the strut circumference based on the skin areas of the strut, namely, downward-facing skin (down), lateral skin (side) and upward-facing skin (up).

Figure 13 reveals the relationship between the area surface roughness around the circumference and the designed strut diameters. For small strut diameters (0.2–0.4 mm), localised peaks on the downward skin are consistent for struts in all inclination angles. This phenomenon becomes less dominant for struts with 0.5–0.7 mm diameters in which the Ra values exhibit irregular fluctuations at the downward-facing areas. For 0.8–1.0 mm struts, the variations of Ra start to exhibit certain level of inconsistency, where struts built in higher inclination angles (50° and 60°) present small fluctuations around 17 μm throughout the circumference of the struts. In contrast, the struts built along 20–40° show

prominent peaks on the downward-facing areas. This indicates that the effect of overhang angle on downward surface roughness is more dominant in thicker struts.

Figure 14 shows relatively uniform roughness over the whole circumference for higher inclination angles. For lower angle struts, localised roughness peaks are perceivable at the downward skin area for all diameters and become less obvious with increasing inclination angle, which aligns well with results present in the literature [9]. For struts built at 60°, the 0.3 mm strut exhibits a relatively large roughness variation compared to other struts, especially around the interface between downward-facing and lateral skin. This is expected based on the previous discussion about the irregularity (Section 3.3.1). Overall, the surface roughness between the downward skin and the side area for higher inclination angles (50° and 60°) exhibits only marginal

Fig. 13 Ra values along the strut circumference plotted in terms of the strut diameters

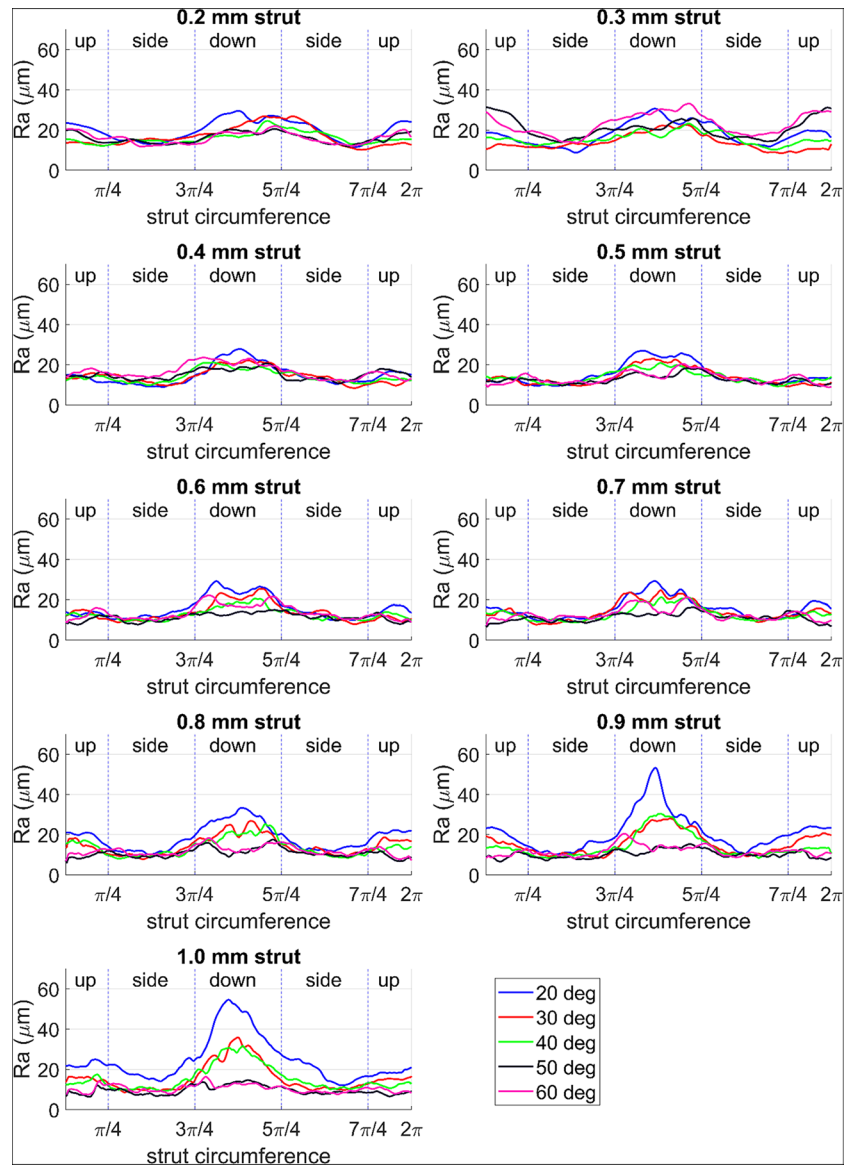
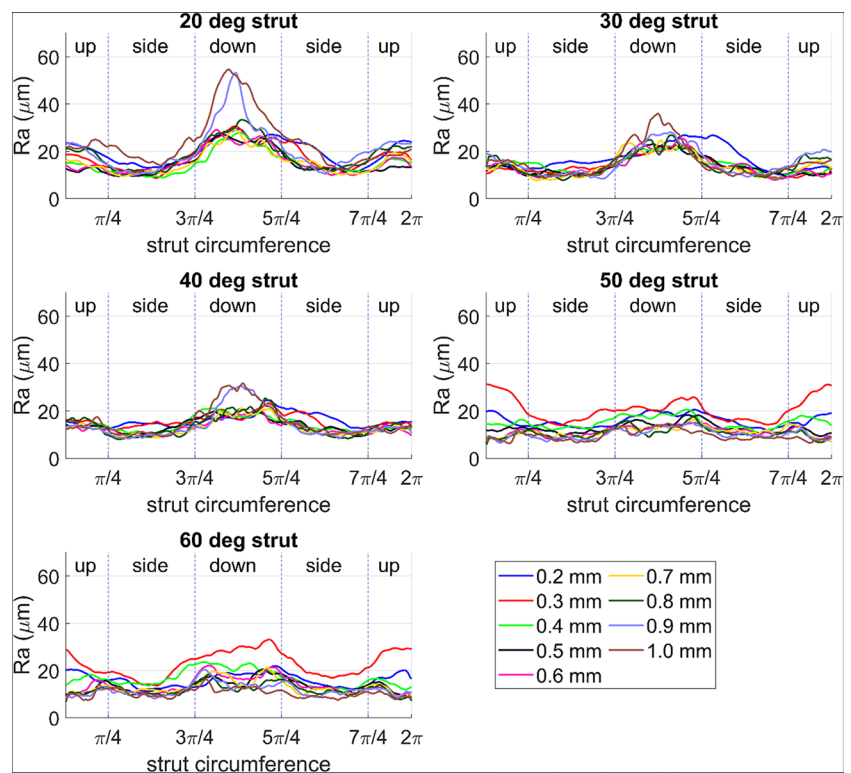


Fig. 14 Ra values along the strut circumference plotted regarding the strut inclination angles



difference (within 10 μm), which indicates a good consistency of roughness over the surface. There are some discrepancies in such surface variations compared to the literature (up to 40 μm) [9], which might be due to the difference in studied materials and processing parameters.

Based on the observation in Figs. 13 and 14, thick struts in lower inclination angles should be avoided in design for the consistent surface quality of lattice struts. Higher inclination angle struts present even surface textures which are more recommended for fabricating lattice structures with uniform surface quality.

3.3.3 Surface stress concentration analysis

Figure 15 takes 60° 0.9 mm strut for an example to illustrate the schematic procedure of stress concentration analysis from segmentation to post-processing. An example of the ‘over-segmentation’ is demonstrated in Fig. 15b. Compared to segmentation after Wolf pruning at 5% (Fig. 15c), the direct watershed transformation provides very dense surface segmentation which leaves out the key features. After Wolf pruning, the surface valleys are separated along the surface peaks (Fig. 15c). The circled valleys are located on the edge of the surface which are removed in the post-processing procedure (Fig. 15c). The reason and influence of the post-processing are discussed below.

Figure 16 presents the global SCFs (see Eq. 4) and maximum local SCFs of all struts. The dashed contour in Fig. 16a–b and d–e represents the mean value in the

category. Figure 16a–c depicts the calculated global and local SCFs and Fig. 16d–e represents the data after post-processing removing all the SCF at the edge of the surface tomography mapping. The reason for such post-processing is to minimise the boundary effect after unfolding in the analytical calculations, which has been reported in the literature [60]. The local valley of a segmented area may sit at the boundary of the tomography surface due to the unfolding process, which contributes to discontinued data at the parting line (being categorised in the upper skin area). This discontinuity could lead to unrealistic results of the curvature calculation at the edge points. The comparison of the post-processed data and the directly calculated results support this assumption and is discussed as follows.

For struts of 0.6–1 mm in diameter, the global SCF declines with an increase of inclination angle (Fig. 16a) whereas for smaller struts (0.2–0.5 mm), the global SCF remains relatively high with a stochastic distribution. To maintain a low and consistent SCF of the LPBF lattice struts, higher inclination angles (greater than 40°) and larger strut diameters (greater than 0.5 mm) are recommended.

An abnormal peak can be noticed in the data which denotes the strut in 60° 0.3 mm configuration in the global SCFs (Fig. 16a and d). The same phenomenon can be seen in the post-processed results of the maximum local SCFs (Fig. 16e). This could be attributed to the influence of the irregularity discussed in the surface tomography mapping (see Section 3.3.1).

Fig. 15 Schematic of stress concentration analysis. **a** Gaussian filtered tomography surface mapping; **b** ‘over-segmented’ tomography surface using watershed transformation; **c** watershed surface after Wolf pruning segmentation

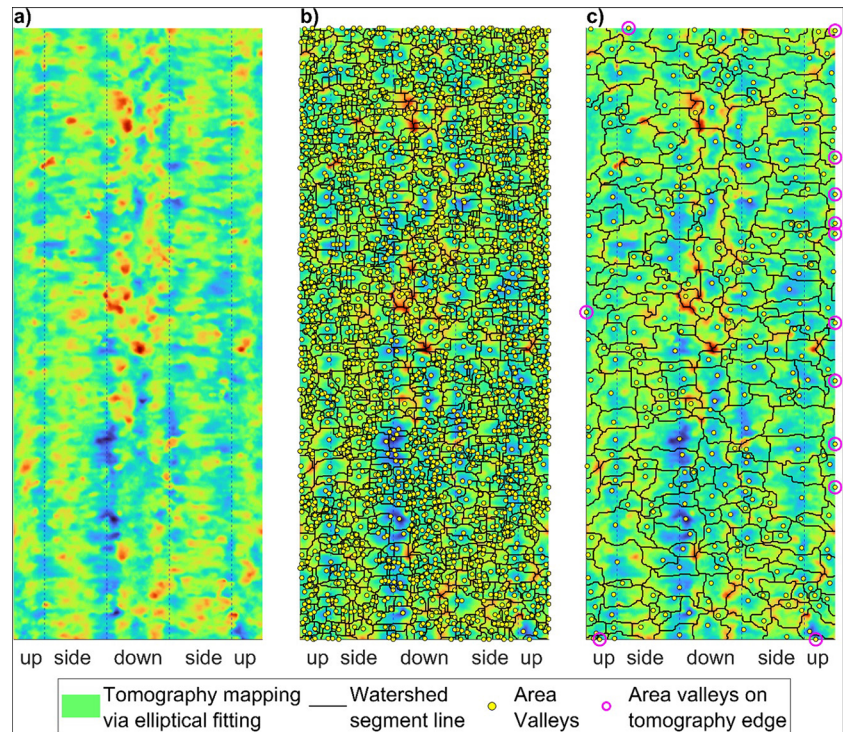
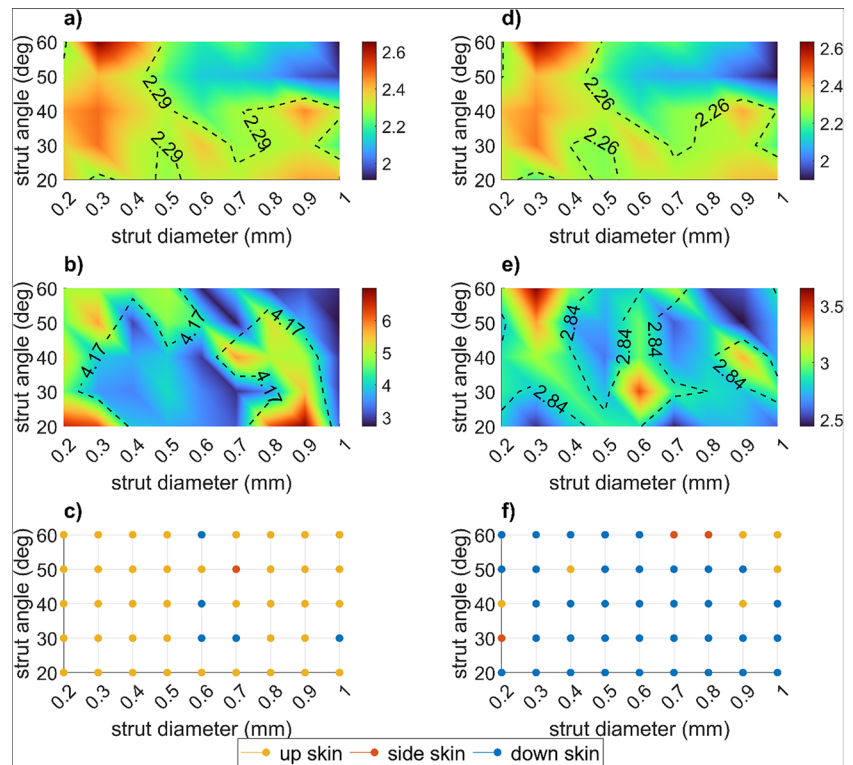


Fig. 16 Analytical stress concentration factors (SCFs) results of all struts computed based on the tomography mapping. **a** Global SCFs; **b** maximum local SCFs; **c** location of maximum local SCFs; **d, e, f** post-processed result with the same layout as **a–c** after removal of all SCF values located at the edge of the tomography mapping



The values of the maximum local SCFs before post-processing (Fig. 16b) are two times higher than that of the global SCFs (Fig. 16a). Most of these critical SCFs appear on the upper surface (Fig. 16c). This seems contradictory to

the previous optical assessments that the upper skins generally present a smooth and shining surface compared to the downside. Moreover, the abnormal peak of 60° 0.3 mm strut discussed earlier is not present in Fig. 16b, indicating that the

boundary effect could be more influential in the calculation of the local SCFs compared to the data irregularity. This suggests that the boundary effect is inevitable due to the unfolding procedure in the surface tomography mapping, which confirms the necessity of the data post-processing.

After post-processing (by removing the valleys on the edges), although the merits of the maximum local SCFs (Fig. 16e) are still over that of the global SCFs (Fig. 16a), the highest value drops by almost half, which is reasonable. Moreover, the locations of maximum local SCFs shifted from the upper skin to the downward-facing area for most of the struts, which aligns with the findings in the surface roughness analysis.

The global SCFs (Fig. 16a and d) exhibit only marginal changes after the post-processing, which indicates that the boundary effect has little influence on them. This might be attributed to their global nature so that the boundary effects, which are local in nature, are very limited. This indicates that the global SCF is more reliable because it is less affected by numerical errors such as the boundary effect. Given that the numerical errors may involve human factors and manipulation that may not be easily diagnosed and corrected properly, the use of global SCF is recommended.

Notably, for struts built along 60° with diameters over 0.6 mm, the location of the maximum local SCF expands to lateral and upward-facing skins. This is different from other inclination angle struts where the maximum local SCF is mostly observed in the downward-facing area. This indicates that the surfaces of these struts tend to have a more uniform texture and roughness along the circumference of the strut, which agrees well with Figs. 13 and 14. As the presence of rough downward-facing skin is associated with the inclination angle, it also implies that the influence of the overhang effect on the as-built surface quality decreases as the inclination angle increases.

Comparing the distribution of the global SCFs with the result of SRPs in 2D and 3D (Figs. 10 and 11), a similar overall tendency can be observed but with a narrower acceptable window. This suggests that the SRPs are insufficient to characterise the surface quality in terms of fatigue. For example, one surface may be prone to fatigue due to the presence of a higher SCF compared to another that has the same measurements of SRPs. This further confirms the necessity of conducting stress concentration analysis to quantitatively evaluate the surface quality.

4 Discussion

4.1 Holistic quantitative evaluation of geometry and surface

μ -CT enables extensive high-resolution characterisation in terms of geometrical, exterior surface and interior features

of small specimens. Despite the advantages of μ -CT, the large amount of CT scan data requires sophisticated algorithms and analyses to convey its full benefits, which challenges conventional data processing techniques. The proposed comprehensive analysis approaches in this study show the potential for an in-depth evaluation of the print quality of LPBF as-built NiTi lattice struts with regard to the geometry and surface features. Such methods provide statistical results beyond the capability of commercial 3D software analysis packages. In this section, the advantage of the proposed analysis will be discussed versus existing analysis approaches in the literature.

The geometric variation analysis is an extension of 2D shape analysis methods. It expanded the cross-section analysis employed in the literature [5, 6, 9, 10] from qualitative analysis to quantitative analysis on geometric deviation. The effective elliptical and circular fittings obtained from this analysis document the geometric discrepancy of lattice struts in shape and size with strong statistical significance. The obtained numerical results are more reliable and accurate compared to other assessments such as SEM and volume difference.

The surface quality analysis consists of three individual evaluation approaches: tomography mapping, surface roughness and stress concentration analyses. The surface tomography mapping presents the advantages of unfolding the as-built geometry into a flat surface providing the fundamentals for the two latter methods. Through this mapping process, the surface texture for all investigated specimens is presented. It allows an intuitive visual assessment of the CT data quality to capture and adjust any irregularity that may occur during the printing process and the scan procedure. The calibration of the data via filtering operation ensures the credibility of the subsequent analysis.

The analysis of surface roughness parameters enables the numerical characterisation of the surface roughness of the manufactured struts in both 3D and 2D. It supports an intuitive assessment of the overall roughness of the as-built surface texture and reveals the relationship between surface roughness and design elements, such as strut diameter and inclination angle. The drawback of this general SRP examination is that it cannot document the surface roughness in specific surface regions. Surface areas such as the downward-facing and upward-facing skins do not necessarily exhibit similar surface roughness [9, 10]. This limitation can be addressed by computing the 2D SPR such as R_a along the circumference of the strut. Moreover, the normalisation of SRP with respect to the strut diameter provides insight into the powder size effect on SRP for thin struts.

The stress concentration analysis predicts the likelihood of fatigue crack initiation and where this may occur. The misalignment of SRP (Figs. 10, 11, 12, 13 and 14) and SCF

(Fig. 16) demonstrates the limitation of using surface texture for evaluating the fatigue cracking of the AM as-built components, which has been pointed out in the literature [14, 18]. Compared to surface roughness analysis, the stress concentration analysis provides a more reliable assessment of fatigue cracking of AM as-built components via computing the stress concentration factors of the topography surface of the struts. The obtained global SCF (1.9–2.6) is comparable with the results (1.25–2.4) reported in the literature [15, 16], which confirms the credibility of this approach. The location of the maximum local SCF after removing edge SCF closely aligns with the results obtained in the previous surface roughness analysis, validating the reliability of this method.

Current analytical estimations of SCF for machined surfaces are either based on sine/cosine wave description of the surface [60, 70] or the simplified 2D profiles according to the tooling periodicity [64]. However, the stochastic surface textures produced by LPBF exhibit high association with the geometry such as the overhang and inclination angle [71]. This makes the existing analytical methods for machined surfaces inapplicable to the LPBF builds. Compared to the use of FEA for precise SCF calculations, the proposed approach based on the surface tomography is more effective in terms of computational cost and time [60]. Although this approach cannot reach the accuracy of FEA, the developed analytical method provides reliable global SCF results, which has not been integrated into any commercial software yet.

To date, a few studies [6–8] have attempted to characterise stress concentration factor of lattice structures as a whole using the maximum von Mises equivalent stress and the nominal homogeneous stress from the FEA model. However, this method requires exhaustive FEA simulations and the calculated SCF ranges from 40 to 90, which misaligns with the commonly accepted definition of SCF. The reason for such overestimated results may be ascribed to the lack of consideration of the stress in individual struts of lattice structures. In comparison, the proposed approach provides more applicable results and can be further extended to evaluate the SCF of struts in lattice structures with different stress modes such as tension and compression. These systematic analyses allow a comprehensive, comparative and quantitative description of the print quality of LPBF as-built NiTi lattice struts.

One limitation of this study is that all specimens examined were manufactured using the same set of LPBF processing parameters. Without necessary modifications, the recommendations proposed in this study may not be directly applicable to other sets of processing parameters. Future evaluation can be performed on specimens produced with different parameter sets, such as the parameter set with the optimised surface roughness, to increase the applicability of the proposed analysis.

4.2 Implications to lattice structure design for fatigue

The print quality assessment of the as-built NiTi lattice struts in various build orientations and strut diameters documents the manufacturing discrepancy from the initial design. In this section, the print quality results obtained via the developed method are compared with those reported in the literature.

From the geometric analysis, one key information extracted is that all manufactured struts are thicker (diameter) than their designed counterparts, which agrees with most studies in the literature [4, 7, 11, 57, 72]. Some work also reported thinner manufactured struts compared to the designed model [5, 9]. This might be related to the ratio between powder particle size and the strut diameter. In this study, the investigated strut diameter is close to the powder size, which is smaller than those reported in the literature. Therefore, powders attached to the struts of smaller diameters have a greater impact on strut geometry than on those of bigger diameters, which can be verified in Fig. 6. The difference in material properties can be another reason [57]. With different materials, the optimal LPBF process parameters vary significantly, which can impact the achievable geometry and mechanical properties [4]. In addition, the melt pool size which is regulated through processing parameters can also contribute to the geometry deviation [67–69]. Although the as-built strut diameter is generally greater than the intended design and the shape is more of an elliptical profile (shape), the size and shape deviations exhibit a converging trend with increasing strut diameter. Based on the geometric analysis, thin struts (diameter < 0.7 mm) should be avoided in the design of lattice structures to maintain a reasonable uniform geometry of the struts (deviation within 20%).

Through the surface tomography mapping, rougher surface textures (Figs. 7 and 8) are noticeable at the downward skin area for all struts as already noted in the literature [10]. This phenomenon is further confirmed by the following surface roughness analysis with the mean height of the surface (R_a) varying between 10 and 20 μm along the circumference (Figs. 13 and 14). The R_a variations between the skin areas around the circumference exhibit a decreasing trend when increasing the inclination angle of the struts, as agreed consistently with previous studies [9, 10]. In this study, localised roughness peaks are perceivable on the downward skin areas for all diameters, in contrast to a previous study which reveals that the lateral skins are the roughest area around the circumference [9]. The presence of unmelted particles attached to the underside due to the overhang effect can contribute to the rough surface in that area. The location of the roughest area may be affected by the printing parameters and powder size. This needs further investigation, but it is beyond the scope of this work.

Table 6 Manufacture quality of the as-built struts via optical assessment and quantitative investigation

| | | Strut diameter (mm) | | | | | | | | | |
|-----------------------------|----|---------------------|-----|-----|-----|-----|-----|-----|-----|-----|--|
| | | 0.2 | 0.3 | 0.4 | 0.5 | 0.6 | 0.7 | 0.8 | 0.9 | 1.0 | |
| Strut inclination angle (°) | 10 | YES | YES | YES | OK | OK | NO | NO | NO | NO | |
| | 20 | YES | YES | YES | YES | YES | YES | OK | OK | OK | |
| | 30 | YES | YES | YES | YES | YES | YES | YES | YES | YES | |
| | 40 | YES | YES | YES | YES | YES | YES | YES | YES | YES | |
| | 50 | YES | YES | YES | YES | YES | Opt | Opt | Opt | Opt | |
| | 60 | YES | YES | YES | YES | YES | Opt | Opt | Opt | Opt | |

‘NO’, ‘OK’ and ‘YES’ stand for the same results from previous optical assessments (Table 3) and ‘Opt’ refers to the optimal manufacturing quality for lattice structures design after quantitative analysis

Notably, the Ra variation range observed on NiTi struts is two times smaller than that of Ti6Al4V which is around 40 μm [9, 10]. This suggests the non-negligible effect of materials on the print surface quality of the LPBF components and the necessity of conducting a manufacturability study on required materials [57]. To avoid large surface roughness discrepancy between areas around the circumference and maintain a relatively smooth surface texture, inclination angles greater than 40° are recommended.

The stress concentration analysis assists the prediction of fatigue crack initiation in the as-built struts. The SCF values calculated on the LPBF NiTi struts are generally two to three times higher compared to the SCF measured on machined surfaces [60, 70, 73]. The critical local SCF is largely located in the downward skin area of the strut, which is consistent with findings reported in another study [15]. The proposed SCF analysis assumes that the notch depth is negligible compared to the thickness of the workpiece. For strut diameters investigated in this study, the notch depth (R_v/S_v) over the fitted diameter ratio ranges from 0.05 to 0.28, meaning that the effective notch depths cannot be neglected. The high ratio of notch depth and strut diameter may lead to inconsistency of the experimental results with the SCF results, which could be minimised by increasing the strut diameter. To prevent crack initiation at areas with high stress concentration, design with a lower and consistent SCF should be considered. Therefore, strut diameters over 0.7 mm and inclination angles greater than 50° are recommended.

The results of the print quality examination provide an exhaustive guideline for future lattice structure design. Compared to the initial intuitive optical assessment, the quantitative evaluation reveals different print windows for manufacturing quality (Table 6), which highlights the importance of conducting statistical analysis.

This approach can be further extended to evaluate the geometric variations and stress concentration factors at the node intersections of lattice struts where stress concentration is more likely to occur as observed in the literature [30]. Furthermore, variable node connection topology (strut number

and orientation) and strut diameter can be investigated to assist more superior lattice design that considers manufacturing limitations and imperfections. In addition, the collected data is easily adaptable for machine learning in the prediction of fatigue cracking in lattice structures.

5 Conclusion

This study has developed a comprehensive approach to characterise the print quality of lattice struts and reveal the relationship between design elements and the print quality of LPBF NiTi lattice struts. More specifically, lattice struts fabricated by LPBF with diameters ranging from 0.2 to 1.0 mm and inclination angles of 10–60° have been quantitatively evaluated in terms of geometric deviations and surface quality. The following conclusion can be drawn:

- The geometric deviation of manufactured lattice struts from their design has a strong correlation with their geometric design in the lattice structure. This deviation decreases with increasing strut diameter and inclination angle.
- The surface texture exhibits non-uniform distribution along the strut circumference, with the downward-facing area presenting a rougher surface compared to other skin areas. This phenomenon becomes less noticeable when increasing the inclination angle over 50°, leading to a surface with more uniform texture distribution.
- The critical stress concentration factors are more prevalent in the downward-facing area. For struts with a diameter over 0.5 mm, the global stress concentration factor decreases as the inclination angle increases.
- The developed analyses extract all the 3D data that a $\mu\text{-CT}$ scan offers, allowing one to determine the precise strut morphology and extract all the surface features. This makes it possible to evaluate geometric characteristics like diameter (size), major and minor axes for elliptical cross-sections (shape), the linear and area surface roughness and the stress concentration factor of the strut surface.

- The results of surface roughness analysis do not necessarily match the stress concentration analysis. Therefore, to better estimate fatigue crack initiation in LPBF lattice structures, it is recommended to use the proposed stress concentration analysis instead of surface roughness results.

Supplementary information The online version contains supplementary material available at <https://doi.org/10.1007/s00170-024-13024-w>.

Acknowledgements This work is supported by a Deakin University start-up funding, Deakin University Postgraduate Research Scholarship (DUPRS). The authors acknowledge the use of the Deakin additive manufacturing facility and the support of the technical staff for manufacturing and EDM cutting the specimens.

Author contribution MZ: conceptualisation, software, methodology, investigation, data curation, validation, formal analysis, writing—original draft, writing—reviewing and editing. KG: conceptualisation, methodology, software, formal analysis, supervision, writing—reviewing and editing. Y-sY: software, formal analysis, writing—reviewing and editing. JE: investigation, writing—reviewing and editing. WX: conceptualisation, methodology, resources, supervision, funding acquisition, writing—reviewing and editing. YW: supervision, project administration, writing—reviewing and editing.

Funding Open Access funding enabled and organized by CAUL and its Member Institutions

Data availability The raw/processed data required to reproduce these findings cannot be shared at this time due to technical or time limitations.

Declarations

Competing interests The authors declare no competing interests.

Open Access This article is licensed under a Creative Commons Attribution 4.0 International License, which permits use, sharing, adaptation, distribution and reproduction in any medium or format, as long as you give appropriate credit to the original author(s) and the source, provide a link to the Creative Commons licence, and indicate if changes were made. The images or other third party material in this article are included in the article's Creative Commons licence, unless indicated otherwise in a credit line to the material. If material is not included in the article's Creative Commons licence and your intended use is not permitted by statutory regulation or exceeds the permitted use, you will need to obtain permission directly from the copyright holder. To view a copy of this licence, visit <http://creativecommons.org/licenses/by/4.0/>.

References

1. Maconachie T, Leary M, Lozanovski B, Zhang X, Qian M, Faruque O, Brandt M (2019) SLM lattice structures: properties, performance, applications and challenges. *Mater Des* 183:108137. <https://doi.org/10.1016/j.matdes.2019.108137>
2. Gibson LJ, Ashby MF (1999) Cellular solids: structure and properties., Second edition, first paperback edition with corrected. Cambridge University Press. <https://doi.org/10.1017/CBO9781139878326>
3. Echeta I, Feng X, Dutton B, Leach R, Piano S (2020) Review of defects in lattice structures manufactured by powder bed fusion. *Int J Adv Manuf Technol* 106:2649–2668. <https://doi.org/10.1007/s00170-019-04753-4>
4. Sing SL, Wiria FE, Yeong WY (2018) Selective laser melting of lattice structures: a statistical approach to manufacturability and mechanical behavior. *Robot Comput-Integr Manuf* 49:170–180. <https://doi.org/10.1016/j.rcim.2017.06.006>
5. Dong Z, Liu Y, Li W, Liang J (2019) Nicolas. *J Alloys Compd* 791:490–500. <https://doi.org/10.1016/j.jallcom.2019.03.344>
6. Dallago M, Raghavendra S, Luchin V, Zappini G, Pasini D, Benedetti M (2021) The role of node fillet, unit-cell size and strut orientation on the fatigue strength of Ti-6Al-4V lattice materials additively manufactured via laser powder bed fusion. *Int J Fatigue* 142:105946. <https://doi.org/10.1016/j.ijfatigue.2020.105946>
7. Dallago M, Winiarski B, Zanini F, Carmignato S, Benedetti M (2019) On the effect of geometrical imperfections and defects on the fatigue strength of cellular lattice structures additively manufactured via selective laser melting. *Int J Fatigue* 124:348–360. <https://doi.org/10.1016/j.ijfatigue.2019.03.019>
8. Dallago M, Fontanari V, Torresani E, Leoni M, Pederzoli C, Potrich C, Benedetti M (2018) Fatigue and biological properties of Ti-6Al-4V ELI cellular structures with variously arranged cubic cells made by selective laser melting. *J Mech Behav Biomed Mater* 78:381–394. <https://doi.org/10.1016/j.jmbbm.2017.11.044>
9. Vanderesse N, Bocher P, Nuño N, Yáñez A, Hof LA (2022) On the characterization of roughness and geometrical irregularities of additively manufactured single titanium-alloy struts. *Addit Manuf* 54:102731. <https://doi.org/10.1016/j.addma.2022.102731>
10. Murchio S, Dallago M, Zanini F, Carmignato S, Zappini G, Berto F, Maniglio D, Benedetti M (2021) Additively manufactured Ti-6Al-4V thin struts via laser powder bed fusion: effect of building orientation on geometrical accuracy and mechanical properties. *J Mech Behav Biomed Mater* 119:104495. <https://doi.org/10.1016/j.jmbbm.2021.104495>
11. Al-Saedi DSJ, Masood SH, Faizan-Ur-Rab M, Alomarah A, Ponnusamy P (2018) Mechanical properties and energy absorption capability of functionally graded F2BCC lattice fabricated by SLM. *Mater Des* 144:32–44. <https://doi.org/10.1016/j.matdes.2018.01.059>
12. Amani Y, Dancette S, Delroisse P, Simar A, Maire E (2018) Compression behavior of lattice structures produced by selective laser melting: X-ray tomography based experimental and finite element approaches. *Acta Mater* 159:395–407. <https://doi.org/10.1016/j.actamat.2018.08.030>
13. Lin C-Y, Wirtz T, LaMarca F, Hollister SJ (2007) Structural and mechanical evaluations of a topology optimized titanium interbody fusion cage fabricated by selective laser melting process. *J Biomed Mater Res A* 83A:272–279. <https://doi.org/10.1002/jbm.a.31231>
14. Vayssette B, Saintier N, Brugger C, El May M (2020) Surface roughness effect of SLM and EBM Ti-6Al-4V on multiaxial high cycle fatigue. *Theor Appl Fract Mech* 108:102581. <https://doi.org/10.1016/j.tafmec.2020.102581>
15. Solberg K, Berto F (2020) The effect of defects and notches in quasi-static and fatigue loading of Inconel 718 specimens produced by selective laser melting. *Int J Fatigue* 137:105637. <https://doi.org/10.1016/j.ijfatigue.2020.105637>
16. Razavi SMJ, Van Hooreweder B, Berto F (2020) Effect of build thickness and geometry on quasi-static and fatigue behavior of Ti-6Al-4V produced by electron beam melting. *Addit Manuf* 36:101426. <https://doi.org/10.1016/j.addma.2020.101426>
17. Ren S, Chen Y, Liu T, Qu X (2019) Effect of build orientation on mechanical properties and microstructure of Ti-6Al-4V

- manufactured by selective laser melting. *Metall Mater Trans A* 50:4388–4409. <https://doi.org/10.1007/s11661-019-05322-w>
18. Persenot T, Burr A, Martin G, Buffiere J-Y, Dendievel R, Maire E (2019) Effect of build orientation on the fatigue properties of as-built electron beam melted Ti-6Al-4V alloy. *Int J Fatigue* 118:65–76. <https://doi.org/10.1016/j.ijfatigue.2018.08.006>
 19. Hacısalihoğlu I, Yıldız F, Çelik A (2021) The effects of build orientation and hatch spacing on mechanical properties of medical Ti-6Al-4V alloy manufactured by selective laser melting. *Mater Sci Eng A* 802:140649. <https://doi.org/10.1016/j.msea.2020.140649>
 20. Tarik Hasib M, Ostergaard HE, Li X, Kruzic JJ (2021) Fatigue crack growth behavior of laser powder bed fusion additive manufactured Ti-6Al-4V: roles of post heat treatment and build orientation. *Int J Fatigue* 142:105955. <https://doi.org/10.1016/j.ijfatigue.2020.105955>
 21. Kanerva M, Pärnänen T, Jokinen J, Haaja J, Ritvanen A, Schlenzka D (2020) Multi-axis fatigue experimentation system of intramedullary implants for femur and tibia. *J Orthop Res* 38:984–995. <https://doi.org/10.1002/jor.24545>
 22. Yang P-F, Sanno M, Ganse B, Koy T, Brüggemann G-P, Müller LP, Rittweger J (2014) Torsion and antero-posterior bending in the in vivo human tibia loading regimes during walking and running. *PLoS ONE* 9:e94525. <https://doi.org/10.1371/journal.pone.0094525>
 23. Liu L, Kamm P, García-Moreno F, Banhart J, Pasini D (2017) Elastic and failure response of imperfect three-dimensional metallic lattices: the role of geometric defects induced by selective laser melting. *J Mech Phys Solids* 107:160–184. <https://doi.org/10.1016/j.jmps.2017.07.003>
 24. Yáñez A, Fiorucci MP, Cuadrado A, Martel O, Monopoli D (2020) Surface roughness effects on the fatigue behaviour of gyroid cellular structures obtained by additive manufacturing. *Int J Fatigue* 138:105702. <https://doi.org/10.1016/j.ijfatigue.2020.105702>
 25. Aboulkhair NT, Everitt NM, Ashcroft I, Tuck C (2014) Reducing porosity in AlSi10Mg parts processed by selective laser melting. *Addit Manuf* 1–4:77–86. <https://doi.org/10.1016/j.addma.2014.08.001>
 26. Van Hooreweder B, Apers Y, Lietaert K, Kruth J-P (2017) Improving the fatigue performance of porous metallic biomaterials produced by selective laser melting. *Acta Biomater* 47:193–202. <https://doi.org/10.1016/j.actbio.2016.10.005>
 27. Wu M-W, Chen J-K, Lin B-H, Chiang P-H (2017) Improved fatigue endurance ratio of additive manufactured Ti-6Al-4V lattice by hot isostatic pressing. *Mater Des* 134:163–170. <https://doi.org/10.1016/j.matdes.2017.08.048>
 28. Mohammadian N, Turenne S, Brailovski V (2018) Surface finish control of additively-manufactured Inconel 625 components using combined chemical-abrasive flow polishing. *J Mater Process Technol* 252:728–738. <https://doi.org/10.1016/j.jmatprotec.2017.10.020>
 29. Persenot T, Burr A, Dendievel R, Buffiere J-Y, Maire E, Lachambre J, Martin G (2020) Fatigue performances of chemically etched thin struts built by selective electron beam melting: experiments and predictions. *Materialia* 9:100589. <https://doi.org/10.1016/j.mtla.2020.100589>
 30. Karami K, Blok A, Weber L, Ahmadi SM, Petrov R, Nikolic K, Borisov EV, Leeftang S, Ayas C, Zadpoor AA, Mehdipour M, Reinton E, Popovich VA (2020) Continuous and pulsed selective laser melting of Ti6Al4V lattice structures: effect of post-processing on microstructural anisotropy and fatigue behaviour. *Addit Manuf* 36:101433. <https://doi.org/10.1016/j.addma.2020.101433>
 31. Lynch ME, Williams K, Cabrera M, Beccuti T (2021) Surface finishing of additively manufactured IN718 lattices by electrochemical machining. *Int J Adv Manuf Technol* 113:967–984. <https://doi.org/10.1007/s00170-020-05699-8>
 32. Mingear J, Zhang B, Hartl D, Elwany A (2019) Effect of process parameters and electropolishing on the surface roughness of interior channels in additively manufactured nickel-titanium shape memory alloy actuators. *Addit Manuf* 27:565–575. <https://doi.org/10.1016/j.addma.2019.03.027>
 33. Urlea V, Brailovski V (2017) Electropolishing and electropolishing-related allowances for powder bed selectively laser-melted Ti-6Al-4V alloy components. *J Mater Process Technol* 242:1–11. <https://doi.org/10.1016/j.jmatprotec.2016.11.014>
 34. British Standards Institution, BS EN ISO 21920-2:2022 (2022) Geometrical product specifications (GPS). Surface texture: profile part 2: terms, definitions and surface texture parameters
 35. British Standards Institution, BS EN ISO 25178-2:2022 (2022) Geometrical product specifications (GPS). Surface texture: areal part 2: terms, definitions and surface texture parameters
 36. Chang S, Liu A, Ong CYA, Zhang L, Huang X, Tan YH, Zhao L, Li L, Ding J (2019) Highly effective smoothing of 3D-printed metal structures via overpotential electrochemical polishing. *Mater Res Lett* 9. <https://doi.org/10.1080/21663831.2019.1601645>
 37. Lee S, Rasoolian B, Silva DF, Pegues JW, Shamsaei N (2021) Surface roughness parameter and modeling for fatigue behavior of additive manufactured parts: a non-destructive data-driven approach. *Addit Manuf* 46:102094. <https://doi.org/10.1016/j.addma.2021.102094>
 38. Leary M, Mazur M, Williams H, Yang E, Alghamdi A, Lozanovski B, Zhang X, Shidid D, Farahbod-Sternahl L, Witt G, Kelbassa I, Choong P, Qian M, Brandt M (2018) Inconel 625 lattice structures manufactured by selective laser melting (SLM): mechanical properties, deformation and failure modes. *Mater Des* 157:179–199. <https://doi.org/10.1016/j.matdes.2018.06.010>
 39. Mazur M, Leary M, McMillan M, Sun S, Shidid D, Brandt M (2017) 5 - Mechanical properties of Ti6Al4V and AlSi12Mg lattice structures manufactured by selective laser melting (SLM). In: M. Brandt (Ed.). *Laser Addit Manuf.*, Woodhead Publishing, pp 119–161. <https://doi.org/10.1016/B978-0-08-100043-3.00005-1>
 40. Mazur M, Leary M, McMillan M, Elambasseril J, Brandt M (2016) SLM additive manufacture of H13 tool steel with conformal cooling and structural lattices. *Rapid Prototyp J* 22:504–518. <https://doi.org/10.1108/RPJ-06-2014-0075>
 41. Mazur M, Leary M, Sun S, Vcelka M, Shidid D, Brandt M (2015) Deformation and failure behaviour of Ti-6Al-4V lattice structures manufactured by selective laser melting (SLM). *Int J Adv Manuf Technol*. <https://doi.org/10.1007/s00170-015-7655-4>
 42. Noronha J, Qian M, Leary M, Kyriakou E, Brandt M (2021) Hollow-walled lattice materials by additive manufacturing: design, manufacture, properties, applications and challenges. *Curr Opin Solid State Mater Sci* 25:100940. <https://doi.org/10.1016/j.cossms.2021.100940>
 43. Melancon D, Bagheri ZS, Johnston RB, Liu L, Tanzer M, Pasini D (2017) Mechanical characterization of structurally porous biomaterials built via additive manufacturing: experiments, predictive models, and design maps for load-bearing bone replacement implants. *Acta Biomater* 63:350–368. <https://doi.org/10.1016/j.actbio.2017.09.013>
 44. Fritsch T, Farahbod-Sternahl L, Serrano-Muñoz I, Léonard F, Haberland C, Bruno G (2021) 3D computed tomography quantifies the dependence of bulk porosity, surface roughness, and re-entrant features on build angle in additively manufactured IN625 lattice struts. *Adv Eng Mater* n/a:2100689. <https://doi.org/10.1002/adem.202100689>
 45. Pérez-Sánchez A, Yáñez A, Cuadrado A, Martel O, Nuño N (2018) Fatigue behaviour and equivalent diameter of single Ti-6Al-4V struts fabricated by electron beam melting orientated

- to porous lattice structures. *Mater Des* 155:106–115. <https://doi.org/10.1016/j.matdes.2018.05.066>
46. Masoumi Khalil Abad E, Pasini D, Cecere R (2012) Shape optimization of stress concentration-free lattice for self-expandable nitinol stent-grafts. *J Biomech* 45:1028–1035. <https://doi.org/10.1016/j.jbiomech.2012.01.002>
 47. Pelton AR, Schroeder V, Mitchell MR, Gong X-Y, Barney M, Robertson SW (2008) Fatigue and durability of nitinol stents. *J Mech Behav Biomed Mater* 1:153–164. <https://doi.org/10.1016/j.jmbbm.2007.08.001>
 48. Chernyshikhin SV, Pelevin IA, Karimi F, Shishkovsky IV (2022) The study on resolution factors of LPBF technology for manufacturing superelastic NiTi endodontic files. *Materials* 15:6556. <https://doi.org/10.3390/ma15196556>
 49. Khademzadeh S, Zanini F, Rocco J, Brunelli K, Bariani PF, Carmignato S (2020) Quality enhancement of microstructure and surface topography of NiTi parts produced by laser powder bed fusion. *CIRP J Manuf Sci Technol* 31:575–582. <https://doi.org/10.1016/j.cirpj.2020.08.009>
 50. Zanini F, Pagani L, Savio E, Carmignato S (2019) Characterisation of additively manufactured metal surfaces by means of X-ray computed tomography and generalised surface texture parameters. *CIRP Ann* 68:515–518. <https://doi.org/10.1016/j.cirp.2019.04.074>
 51. Zanini F, Sbettega E, Sorgato M, Carmignato S (2019) New approach for verifying the accuracy of X-ray computed tomography measurements of surface topographies in additively manufactured metal parts. *J Nondestruct Eval* 38:12. <https://doi.org/10.1007/s10921-018-0547-4>
 52. Rott S, Ladewig A, Friedberger K, Casper J, Full M, Schleifenbaum JH (2020) Surface roughness in laser powder bed fusion – interdependency of surface orientation and laser incidence. *Addit Manuf* 36:101437. <https://doi.org/10.1016/j.addma.2020.101437>
 53. Yang S, Chu C, Tulloh A, Chen F (2021) DCM - a software platform for advanced 3D materials modelling, characterisation and visualization. <https://doi.org/10.25919/6z8c-a014>
 54. Yang YS, Trinchi A, Tulloh A, Chu C (2016) A tutorial introduction to DCM quantitative characterization and modelling of material microstructures using monochromatic multi-energy X-ray CT. *AIP Conf Proc* 1696:020029. <https://doi.org/10.1063/1.4937523>
 55. Yang Y (2018) Data-constrained modelling of material microstructures and properties. *Res Dev Mater Sci* 5. <https://doi.org/10.31031/RDMS.2018.05.000611>
 56. Yang Y, Wang H, Wang J, Wang R, Li J, Liu R (2022) Microstructure characterization of a stainless-steel sample with data-constrained modelling. *J Shanxi Univ* 45:693–700. <https://doi.org/10.13451/j.sxu.ns.2021153>
 57. Jam A, du Plessis A, Lora C, Raghavendra S, Pellizzari M, Benedetti M (2022) Manufacturability of lattice structures fabricated by laser powder bed fusion: a novel biomedical application of the beta Ti-21S alloy. *Addit Manuf* 50:102556. <https://doi.org/10.1016/j.addma.2021.102556>
 58. British Standards Institution, BS EN ISO 25178-1:2016 (2016) Geometrical product specifications (GPS). Surface texture: areal part 1: indication of surface texture
 59. Technical Committee CTN 82 Metrology and calibration (2013) Geometrical product specifications (GPS). Surface texture: areal part 3: specification operators (ISO 25178-3:2012)
 60. Perez I, Madariaga A, Arrazola PJ, Cuesta M, Soriano D (2021) An analytical approach to calculate stress concentration factors of machined surfaces. *Int J Mech Sci* 190:106040. <https://doi.org/10.1016/j.ijmecsci.2020.106040>
 61. Pilkey WD, Peterson RE (1997) Peterson's stress concentration factors, 2nd edn. Wiley, New York
 62. Lou S, Pagani L, Zeng W, Jiang X, Scott PJ (2020) Watershed segmentation of topographical features on freeform surfaces and its application to additively manufactured surfaces. *Precis Eng* 63:177–186. <https://doi.org/10.1016/j.precisioneng.2020.02.005>
 63. British Standards Institution (2013) Geometrical product specifications (GPS). Filtration part 85: morphological areal filters: segmentation (ISO 16610-85:2013)
 64. Quan F, Chen Z, Ye H, Cui C, Cui Y (2021) Study of the effect of surface roughness on fatigue strength of GH4169 based on indirect evaluation of the notch root radius. *Int J Fatigue* 152:106440. <https://doi.org/10.1016/j.ijfatigue.2021.106440>
 65. Masiagutova E, Cabanettes F, Sova A, Cici M, Bidron G, Bertrand P (2021) Side surface topography generation during laser powder bed fusion of AlSi10Mg. *Addit Manuf* 47:102230. <https://doi.org/10.1016/j.addma.2021.102230>
 66. Dallago M, Raghavendra S, Luchin V, Zappini G, Pasini D, Benedetti M (2019) Geometric assessment of lattice materials built via selective laser melting. *Mater Today Proc* 353–361. <https://doi.org/10.1016/j.matpr.2018.11.096>
 67. Aboulkhair NT, Maskery I, Tuck C, Ashcroft I, Everitt NM (2016) On the formation of AlSi10Mg single tracks and layers in selective laser melting: microstructure and nano-mechanical properties. *J Mater Process Technol* 230:88–98. <https://doi.org/10.1016/j.jmatprotec.2015.11.016>
 68. Zhang B, Coddet C (2016) Selective laser melting of iron powder: observation of melting mechanism and densification behavior via point-track-surface-part research. *J Manuf Sci Eng* 138:051001. <https://doi.org/10.1115/1.4031366>
 69. Cloots M, Uggowitzer PJ, Wegener K (2016) Investigations on the microstructure and crack formation of IN738LC samples processed by selective laser melting using Gaussian and doughnut profiles. *Mater Des* 89:770–784. <https://doi.org/10.1016/j.matdes.2015.10.027>
 70. Cheng Z, Zhang Y, Sun X, Wang T, Li S (2020) Stress concentration of 3-D surfaces with small undulations: analytical solution. *Int J Solids Struct* 206:340–353. <https://doi.org/10.1016/j.ijsolstr.2020.09.027>
 71. Leary M, Mazur M, Elambasseril J, McMillan M, Chirent T, Sun Y, Qian M, Easton M, Brandt M (2016) Selective laser melting (SLM) of AlSi12Mg lattice structures. *Mater Des* 98:344–357. <https://doi.org/10.1016/j.matdes.2016.02.127>
 72. Han C, Yan C, Wen S, Xu T, Li S, Liu J, Wei Q, Shi Y (2017) Effects of the unit cell topology on the compression properties of porous Co-Cr scaffolds fabricated via selective laser melting. *Rapid Prototyp J* 23:16–27. <https://doi.org/10.1108/RPJ-08-2015-0114>
 73. Wu ZR, Wang SQ, Yang X, Pan L, Song YD (2021) Fatigue life prediction for Ni-based superalloy GH4169 considering machined surface roughness and residual stress effects. *J Theor Appl Mech* 215–226. <https://doi.org/10.15632/jtam-pl/132951>

Publisher's Note Springer Nature remains neutral with regard to jurisdictional claims in published maps and institutional affiliations.